SANDIA REPORT

SAND2002-2240
Unlimited Release
Printed September 2002

ALEGRA Validation Studies for Regular, Mach, and Double Mach Shock Reflection in Gas Dynamics

Mary I. Chen and Timothy G. Trucano

Prepared by
Sandia National Laboratories
Albuquerque, New Mexico 87185 and Livermore, California 94550

Sandia is a multiprogram laboratory operated by Sandia Corporation, a Lockheed Martin Company, for the United States Department of Energy under Contract DE-AC04-94AL85000

Issued by Sandia National Laboratories, operated for the United States Department of Energy by Sandia Corporation.

Available to DOE and DOE contractors from
U.S. Department of Energy
Office of Scientific and Technical Information
P.O. Box 62
Oak Ridge, TN 37831

Telephone: (865)576-8401
Facsimile: (865)576-5782
E-Mail: reports@adonis.osti.gov
Online ordering: http://www.doe.gov/bridge

Available to the public from
U.S. Department of Commerce
National Technical Information Service
5285 Port Royal Rd
Springfield, VA 22161

Telephone: (800)553-6847
Facsimile: (703)605-6900
E-Mail: orders@ntis.fedworld.gov
Online order: http://www.ntis.gov/ordering.htm

SAND2001-2240
Unlimited Release
Printed September 2002

ALEGRA Validation Studies for Regular, Mach, and Double Mach Shock Reflection in Gas Dynamics

Mary I. Chen
Computational Physics R&D

Timothy G. Trucano
Optimization and Uncertainty Estimation

Sandia National Laboratories
P. O. Box 5800
Albuquerque, New Mexico 87185-0819

Abstract

In this report we describe the performance of the ALEGRA shock wave physics code on a set of gas dynamic shock reflection problems that have associated experimental pressure data. These reflections cover three distinct regimes of oblique shock reflection in gas dynamics – regular, Mach, and double Mach reflection. For the selected data, the use of an ideal gas equation of state is appropriate, thus simplifying to a considerable degree the task of validating the shock wave computational capability of ALEGRA in the application regime of the experiments. We find good agreement of ALEGRA with reported experimental data for sufficient grid resolution. We discuss the experimental data, the nature and results of the corresponding ALEGRA calculations, and the implications of the presented experiment – calculation comparisons.

Acknowledgements

The authors would like to thank Edward Boucheron, Daniel Carroll, Mark Christon, Christopher Garasi, Marlin Kipp, and Allen Robinson for reading and commenting on the manuscript prior to publication.

Contents

Abstract 3
Acknowledgements 4
Contents 5
List of Figures 7
List of Tables 11
1. Introduction 13
2. Description of Calculations and Experimental Data 17
2.1 Description of the Calculations 17
2.1.1 Oblique Shock Reflection 17
2.1.1.1 Regular Shock Reflection 19
2.1.1.2 Mach Reflection 22
2.1.1.3 Double Mach Reflection 24
2.1.2 Geometry, Grid, and Initial Conditions 25
2.1.3 Example Calculations 31
2.1.3.1 Regular Shock Reflection 31
2.1.3.2 Mach Shock Reflection 33
2.1.3.3 Double Mach Shock Reflection 35
3. Comparison With Experimental Data 43
3.1 Summary of Experimental Data 43
3.2 Comments on Validation Metrics 46
3.3 Agreement With Trends and Partial Quantitative Comparisons 48
3.4 Computational Pressure Ratio Variability 51
3.5 Calculation Verification and Computational Uncertainty 58
3.5.1 Convergence 58
3.5.2 Comparison Difficulties 60
3.5.3 Plot Sensitivity 62
4. Discussion 65
References 67
Appendix A: Traceability Information 69
A.1 Mesh Generation 69
A.2 ALEGRA Input 70
A.3 Post-Processing Discussion 72

(Page Left Blank

List of Figures

Figure 2.1 Schematics of possible shock reflection structures: (a) regular reflection; (b) single Mach reflection; and (c) double Mach reflection. This figure is redrawn from Sandoval (1987) with the same orientation as the ALEGRA calculations summarized in this document. 20
Figure 2.2 Geometry of the two-shock theory for regular shock reflection. 21
Figure 2.3 Geometry of the three-shock theory for Mach shock reflection. 23
Figure 2.4 Sample of the initial data and geometry for ALEGRA Eulerian calculations of shock reflection from an oblique planar surface. The regions are effectively of infinite depth into the page because of the assumed Cartesian x – y geometry of these calculations. 26
Figure 2.5 Schematic of the computational geometry and labeled sides for CUBIT meshing specifications. 27
Figure 2.6 Example of the computational mesh in the region of shock formation, propagation, and reflection. 29
Figure 2.7 Sample (a) pressure and (b) density plot with contours (drawn but not labled) for regular shock reflection calculation with a Mach number of 1.37 and incident angle of 35 degrees at a calculation time of 0.7 s. The arrow correlates this figure with the plot in Figure 2.9. 32
Figure 2.8 Sample gradient of the (a) pressure and (b) density plot with contours for regular shock reflection calculation with a Mach number of 1.37 and incident angle of 35 degrees at 0.7 s. The arrow correlates this figure with the plot in Figure 2.9. . 32
Figure 2.9 (a) Pressure plot with distance measured along the face of the wedge in the flow direction for the regular shock reflection calculation with a Mach number of 1.37 and incident angle of 35 degrees. (b) Zoom of the plot over the region indicated by the dotted rectangle in plot (a). 33
Figure 2.10 Sample (a) pressure and (b) density plot with contours for Mach shock reflection calculation with a Mach number of 1.37 and incident angle of 50 degrees at 0.7 s. The arrow correlates this figure with the plot in Figure 2.12. 34
Figure 2.11 Sample gradient of the (a) pressure and (b) density plot with contours for Mach shock reflection calculation with a Mach number of 1.37 and incident angle of 50 degrees at 0.7 s. The arrow correlates this figure with the plot in Figure 2.12. 34
Figure 2.12 (a) Pressure plot with distance measured along the face of the wedge in the flow direction for the Mach shock reflection calculation with a Mach number of 1.37 and incident angle of 50 degrees. (b) Zoom of the plot over the region indicated by the dotted rectangle in plot (a). 35
Figure 2.13 Sample (a) pressure and (b) density plot with contours for double Mach shock reflection calculation with a Mach number of 3.36 and incident angle of 45 degrees at 0.7 s. The arrow correlates this figure with the plot in Figure 2.16. 36
Figure 2.14 Enlarged view of sample (a) pressure and (b) density plot with contours for the double Mach shock reflection calculation with a Mach number of 3.36 and

incident angle of 45 degrees at 0.7 s. The arrow correlates this figure with the plot in Figure 2.16. 36
Figure 2.15 Sample gradient of the (a) pressure and (b) density plot with contours for double Mach shock reflection calculation with a Mach number of 3.36 and incident angle of 45 degrees at 0.7 s. The arrow correlates this figure with the plot in Figure 2.16. 37
Figure 2.16 (a) Pressure plot with distance measured along the face of the wedge in the flow direction for the double Mach shock reflection calculation with a Mach number of 3.36 and incident angle of 45 degrees. (b) Zoom of the plot over the region indicated by the dotted rectangle in plot (a). 37
Figure 2.17 Sample (a) pressure and (b) density plot with contours for double Mach shock reflection calculation with a Mach number of 3.36 and incident angle of 50 degrees. 38
Figure 2.18 Sample gradient of the (a) pressure and (b) density plot with contours for double Mach shock reflection calculation with a Mach number of 3.36 and incident angle of 50 degrees. 39
Figure 2.19 Pressure – distance plots versus wedge angle for (a) M=1.37 and (b) M=3.36 at 0.7 seconds calculation time. 39
Figure 2.20 Top row: Plot of (a) pressure and (b) density along the row of cells just below the boundary between Block 1 and 2 (Fig 2.3) versus time. Bottom row: the percent relative error in the (c) pressure and (d) density, when compared to the initial condition. 40
Figure 2.21 Plot of total energy vs time in the Mach 3.36 calculation with a wedge angle of 45 degrees (a) and the percent error in the total energy when compared to the initial conditions. 41
Figure 2.22 (a) Schematic of where the plot was taken for the pressure versus distance plot and (b) the pressure vs distance plot at three different times. 42
Figure 3.1 Plot of experimental data and analytic theory for Mach 1.37 experiments. This figure is a reproduction of a figure in Sandoval (1987) and has multiple sets of experimental data included. This is why there are multiple experimental data for incident angles between 40 and 45 degrees. 44
Figure 3.2 Plot of experimental data and analytic solution for Mach 3.36 calculation. As in Figure 3.1 this figure is a reproduction of an identical figure in Sandoval (1987). There are multiple sets of experimental data included. The range of incidence angles greater than 40 degrees has multiple pressure data corresponding to the presence of two Mach stems in the experiments. 45
Figure 3.3 Plot of ALEGRA calculation results, experimental data and analytic solution for Mach 1.37 calculation at various incidence angles. 49
Figure 3.4 Plot of ALEGRA calculation results, experimental data and analytic solution for Mach 3.36 calculation at various incidence angles. 50
Figure 3.5 Zoom of the pressure plot along the wedge for the regular reflection problem with Mach number of 1.37 and incident angle of 35 degrees. 52
Figure 3.6 Plot of (a) ALEGRA calculated $R^{(1)}$ and experimental data with the error bars and (b) the corresponding percent relative error for the regular reflection, Mach 1.37

calculation with an incident angle of 35 degrees. We have shown graphically how e and D are defined in (a). 53
Figure 3.7 Zoom of the pressure plot for the Mach shock reflection calculation with a Mach number of 1.37 and incident angle of 50 degrees. 54
Figure 3.8 Plot of (a) experimental data with the error bars and ALEGRA and (b) the percent error for the Mach reflection, Mach 1.37 calculation with an incident angle of 50 degrees. 55
Figure 3.9 Zoom of the pressure plot for the double Mach shock reflection calculation with a Mach number of 3.36 and incident angle of 45 degrees. 56
Figure 3.10 Plot of (a) experimental data with the error bars and ALEGRA calculations and (b) the percent error for the double Mach reflection, Mach 3.36 calculation with a wedge angle of 45 degrees. 57
Figure 3.11 Plot of pressure plots of the regular reflection calculation with Mach number 1.37 and wedge angle 35 degrees for coarse, medium, and fine grids. 59
Figure 3.12 Plot of pressure versus distance of the regular reflection calculation with Mach number 1.37 and wedge angle 50 degrees for coarse, medium, and fine grids. 60
Figure 3.13 Plot of pressure versus distance of the regular reflection calculation with Mach number 3.36 and wedge angle 45 degrees for coarse, medium, and fine grids. 61
Figure 3.14 (a) Pressure versus position plots along the wedge for mach 1.37 calculation with incidence angles of 35 degrees and 35.98 degrees. (b) The comparison of experimental data with the same calculations. 62
Figure 3.15 Pressure versus position plots along the wedge for the Mach 1.37 RR calculation with incident angle 35 degrees at various positions: surface of wedge, 2 zone offset, and 4 zone offset. 63
Figure 3.16 Pressure versus position plots along the wedge for the Mach 1.37 MR calculation with incidence angle 50 degrees at various positions: surface of wedge, 2 zone offset, and 4 zone offset. 63
Figure 3.17 Pressure versus position plots along the wedge for the Mach 3.36 DMR calculation with incidence angle 45 degrees at various positions: surface of wedge, 2 zone offset, and 4 zone offset. 64

(Page Left Blank

List of Tables

Table 2.1 Meshing Scheme. 28
Table 2.2 Initial Conditions for Block 1 30
Table 2.3 Initial Conditions for Block 2 30
Table 3.1 Summary of nominal computational pressure ratios. 51

(Page Left Blank

1. Introduction

A validation assessment activity that is important for applications of the ALEGRA shock wave physics code (Summers, *et al*., 1997) to High Energy Density Physics (HEDP) is to assess validation of the code for strong shock wave applications. While such an assessment contributes to overall validation of application of ALEGRA in a variety of shock hydrodynamics applications, success in this endeavor is far from sufficient for achieving appropriate confidence in compressible multi-material shock wave simulations for complex HEDP applications. It is the purpose of this document to present the results of an ALEGRA validation assessment activity that studies the performance of the code for strong gas dynamic shock waves, thus providing one additional component of needed validation.

The Phenomena Identification and Ranking Table (PIRT) concept is recommended by the Sandia ASCI V&V program for organizing validation assessment activities (Pilch *et al.*, 2000). In unpublished work (Mehlhorn, *et al*., 2000) a PIRT has been partially developed for ALEGRA HEDP applications. The main elements of this PIRT which are relevant to shock hydrodynamics are:

I. **Strong shock waves in multi-material and multi-dimensional hydrodynamics.**

II. **Strong shock waves in multi-material and multi-dimensional magnetohydrodynamics (MHD).**

III. **Strong shock waves in multi-material and multi-dimensional radiation-hydrodynamics (rad-hydro).**

IV. **Strong shock waves in multi-material and multi-dimensional radiation-magnetohydrodynamics (rad-MHD).**

By "strong shock waves" we mean shock waves in which compressibility and high temperatures are important. For example, in an ideal gas a shock velocity that is larger than the sound speed of the ambient gas typically defines a strong shock. We thus distinguish validation assessment for strong shock waves from validation assessment aimed at lower pressure shock waves, which is required for explosively driven component applications of ALEGRA. While strong shock validation assessment may also provide assessment for lower pressure applications, the reverse is not true. It is implicit in our discussion that "strong shock wave" also includes the kind of smooth flows that might be important in the associated applications, such as power driven material expansion (exploding wires, for example).

The PIRT methodology also addresses the importance of validation activities and the believed current capability of the code, in this case ALEGRA, for accurately performing such calculations. All of the items I – IV are of highest priority for HEDP applications of ALEGRA. No such application can be performed in the absence of measured credibility for ALEGRA strong shock wave calculations. We currently believe that ALEGRA is capable of accurately modeling problems in element I, while elements II – IV represent areas of rapidly evolving code capability. Thus, validation assessment of element I has a degree of confirmation associated with it, while validation assessment in the other elements is presently exploratory. The work reported in this document is fully directed at PIRT element I above.

Under the major shock hydrodynamics PIRT element I above there are several other specific elements. These are:

I-a. Single fluid, 1-D.

I-b. Multi-fluid, 1-D.

I-c. Single fluid, 2-D.

I-d. Multi-fluid, 2-D.

I-e. Single fluid, 3-D.

I-f. Multi-fluid, 3-D.

The current work addresses item I-d. All of the elements I-a through I-f potentially require validation assessment for all of the numerical hydrodynamics currently implemented in ALEGRA – (I-d-1) pure Lagrangian, (I-d-2) pure Eulerian, (I-d-3) Arbitrary Lagrange-Eulerian (ALE), and (I-d-4) Adaptive Mesh Refinement (AMR) in the case of element I-d above. We believe that the multi-fluid elements and multi-dimensional elements have higher importance than single fluid or 1-D. Nonetheless it is difficult to completely isolate single fluid from multi-fluid and 1-D from higher dimensional elements. In the absence of specific guidance from the intended application as to the particular numerical hydrodynamics to apply, this leads to a total of twenty-four different assessment activities under the single major PIRT element I; or to ninety-six for all four major elements aimed strictly at assessing shock wave modeling capability of ALEGRA. This is a very large number of potential validation assessment activities.

We observe that our effort in strong shock validation assessment is significantly simplified by the fact that for more specific HEDP applications the relevant numerical hydrodynamics choices are sometimes somewhat restricted. Only those restricted choices are really of concern for validation for that particular application. In addition, if more than one numerical hydrodynamics option must be assessed, we may be able to adequately assess it through the verification exercise of comparing with an option that has already undergone a significant validation assessment. This is the approach that underlies the present work. The direct validation assessment activity we perform is on item I-d, for

Eulerian numerical hydrodynamics. Assessment of pure Lagrangian hydrodynamics is not an option for multi-dimensional strong shock reflection problems because we know from past experience that Lagrangian calculations will not function properly. On the other hand, ALE and AMR are both of interest for strong shock problems, as well as Eulerian. The present work, which emphasizes suitably resolved Eulerian calculations, then can serve as a verification benchmark for future analyses of the application of ALE and AMR to shock reflection problems. We believe Eulerian, ALE, and AMR numerical hydrodynamic options are all expected to be viable options for Z-pinch HEDP applications other than ICF capsule design. Thus, questions about how to appropriately balance validation assessment activities, such as strong shock wave reflection studies, for all three numerical hydrodynamics options are not moot.

To summarize, this report is focused on a validation assessment activity targeted at the specific PIRT element (I-d-2), Eulerian multi-material, two-dimensional strong shock hydrodynamics. To this purpose, Sandoval (1987) reported a set of interesting gas dynamic shock reflection calculations and experimental data that we believe are also useful for studying with ALEGRA. The purpose of Sandoval's study was to validate the capability of the Godunov ALE code CAVEAT (Addessio, *et al*., 1986) for performing the task of computing shock reflections. Although ALEGRA is not a compressible computational fluid dynamics code of the type typically applied to problems of this nature (see Toro, 1999), and an artificial viscosity-based numerical shock hydrodynamics is used rather than a Godunov scheme, the shock reflection problems studied by Sandoval should still provide a reasonable opportunity to gauge the success or failure of ALEGRA for shock wave reflection calculations. It is with this purpose in mind that we present the results in this report.

Sandoval compares shock reflection calculations versus experimental data for three different regimes of shock reflection from planar (Cartesian x – y geometry) oblique surfaces – ***regular shock reflection (RR)***, ***Mach shock reflection (MR)***, and ***double Mach shock reflection (DMR)***. What is most important to us in Sandoval's work is the reported experimental data. We will discuss these data below. In addition, a fairly well developed theory of shock reflection in ideal gases exists (Ben-Dor, 1992) which provides an interesting counterpoint to the calculation – experiment comparisons that we present. We will also review this theory briefly.

The calculations we present are somewhat demanding, since the resolution required to even qualitatively represent the shock wave structures observed in shock reflection transition experiments is quite high for an artificial viscosity code. Nonetheless, an understanding of the required resolution is very useful for other applications of ALEGRA, and this is one of the most interesting features of the work we report here.

In Section 2 we discuss the phenomenology of shock reflection in planar oblique geometry. Then we present the computational approach we apply, including the geometry, meshing, important input variables, and other features necessary to understand and repeat these calculations.

Section 3 presents a comparison of computations performed on the three major classes of shock wave reflection problems (that we discuss in Section 2) with experimental data. We review the experimental data, especially the reported error bars. We also discuss the validation metrics defined for the comparison of the calculations with the chosen experimental data that we apply in this study. The most desirable metric is that the calculations, especially when represented by summary statistics, fall within the data error bars. We also believe that it is of importance to successfully predict the reflection transition regions from regular to Mach or double Mach reflection, which was the underlying motivation for our computational study. Finally, we discuss some results on calculation verification, in particular the grid convergence studies that we performed to arrive at the numerical resolution that was required to achieve reasonable agreement with the experimental data.

We conclude with a discussion of these results, as well as the opportunity for future work, in Section 4. Appendix A provides traceability and repeatability information for these calculations, in particular input deck echoes for mesh generation and ALEGRA, as well as information about the approach used for post-processing our results.

We assume that the reader of this report has familiarity with shock wave physics and the standard methodologies for performing computational simulations in that field.

2. Description of Calculations and Experimental Data

2.1 Description of the Calculations

ALEGRA (Summers, *et al*., 1997) is a multi-material, multi-physics Arbitrary Lagrange Eulerian (Peery and Carroll, 2000) shock wave physics code. This computer code uses a finite element grid for spatial discretization and a matched time-stepping method for performing shock wave physics calculations (Hughes, 1987). Most importantly, ALEGRA uses artificial viscosity for fitting shock waves (Richtmyer and Morton, 1967) in numerical solutions. The artificial viscosity methodology has historical application in both Lagrangian and Eulerian multi-material shock wave calculations. Artificial viscosity provides flexibility for simulating the multitude of shock waves that are expected in general multi-material shock wave physics applications. However, the use of artificial viscosity is also accompanied by the penalty of more stringent requirements for suitable resolution of complex shock structures. Typical artificial viscosity implementations smear shocks over at least four zones in general purpose shock wave physics codes, although the less generally applied algorithm of Christensen (see Benson, 1992 for a discussion and extension of Christensen's ideas) allows shocks to smear over fewer zones. One of the questions that we attempt to answer in this work is what resolution is necessary to achieve sufficient resolution in ALEGRA shock wave calculations using the current artificial viscosity formulation (a combination of linear and quadratic viscosities). This question will be addressed by the work we present in this document.

In the validation assessment activity that we discuss, we examine physical problems in which complex multi-wave structures arise. However, the nature of these chosen problems is typically less complicated than what we might expect from HEDP applications. For example, the shock waves we study in this report can be modeled using ideal gas equations of state. In addition, the overall geometry of the problems is less complex than that found in other applications of interest to us, which also typically require multi-material calculations. The shock structures that result from oblique shock reflection in ideal gases are described in Sandoval (1987) and carefully analyzed in detail in Ben-Dor (1992). An older classic reference is Courant and Friedrichs (1948). Below, we review enough of the phenomenology of shock reflection to make our discussion of the corresponding ALEGRA calculations comprehensible. The interested reader is especially advised to refer to the book of Ben-Dor, as well as the other detailed references given below, to have a more complete picture of this problem.

2.1.1 Oblique Shock Reflection

We will discuss calculations in three distinct regimes of oblique shock reflection below. These regimes – ***regular shock reflection (RR)***, ***Mach shock reflection (MR)***, and ***double Mach shock reflection (DMR)*** – are schematically depicted in Figure 2.1. There

are several important features in these schematic flow fields that are important to understand and which we will now summarize. Our notation is almost identical to that used by Sandoval (1987), although the orientation of the reflection in Figure 2.1 is different than in that work. Our schematic diagrams are fully compatible with the calculations we report, which should make the task of correlating the schematics with the computational diagrams easier for the reader.

Our discussion below assumes ideal gases. The relevant equation of state for ideal gases as implemented in ALEGRA is worth recalling. The equations are

$$\begin{aligned} p &= \rho(\gamma - 1)(I - I_{ref}) \\ T &= \frac{(I - I_{ref})}{C_v} \\ C &= \sqrt{\frac{\gamma p}{\rho}} \end{aligned} \tag{2.1}$$

In equation (2.1) the meaning of the variables is p is pressure, T is temperature, I is the specific internal energy, C is the sound speed, I_{ref} is the reference specific internal energy that allows adjustment of the zero of energy in calculations, and ρ is density. The constant volume heat capacity C_v and the polytropic gas constant γ are input parameters in ALEGRA that uniquely specify the ideal gas. All of the calculations, theory, and experiments discussed in this work assume that $\gamma = 1.4$, a value appropriate for air at conditions that are not extreme enough to trigger real gas effects such as ionization and dissociation. The heat capacity is adjusted to define initial conditions that match those presented in the report of Sandoval (1987). These will be discussed in detail in Section 2.2. All units in this document are cgs (centimeters – grams – seconds). Thus, pressure is measured in dynes/cm^2, and specific internal energy is ergs/g. Temperature is measured in Kelvin.

We consider experimental data on the three different types of shock reflection (RR, MR, and DMR) in this report. The reader should consult the book of Ben-Dor (1992) for further information. We will first describe each of these reflection regimes to provide a self-contained perspective on the comparisons that we will present in this document.

2.1.1.1 Regular Shock Reflection

The case of regular shock reflection (RR) is diagrammed in Figure 2.l(a). The key features in this diagram are the incident shock, assumed to be steady, and the reflected shock "R". The pre-shock conditions of the gas are labeled with the subscript "0". The incident shock wave is assumed to be steady. Then, knowledge of the incident shock velocity, v_s, and the pre-shock gas conditions is sufficient to determine the post-shock gas state, which we label with the subscript "—", through application of the Hugoniot jump conditions (Harlow and Amsden, 1970):

$$\begin{aligned}
\frac{u_-}{C_0} &= \frac{2\left(M^2-1\right)}{(\gamma+1)M} \\
\frac{\rho_-}{\rho_0} &= \frac{\gamma+1}{\gamma-1+\left(2/M^2\right)} \\
\frac{p_-}{p_0} &= 1+\frac{2\gamma}{\gamma+1}\left(M^2-1\right) \\
I_- - I_{ref} &= \frac{p_-}{\rho_-(\gamma-1)}
\end{aligned} \tag{2.2}$$

The Mach number M in (2.2) is defined as $M = v_s/C_0$, where v_s is the shock wave speed. u_- is the material velocity behind the shock, in the direction of motion of the shock (always planar in this report). The material velocity of the pre-shock state in the experiments we consider is zero. The incident shock wave produces a state of uniaxial strain behind it, except in the reflection region, where the flow field is more complex.

The polytropic gas constant, the incident shock wave Mach number, and the angle of the wedge θ_W, or the incident angle of the shock wave $\theta_I = 90° - \theta_W$, define the type of shock reflection that occurs for ideal gases. For certain conditions, this reflection will be regular. An approximate analytical theory that describes regular shock reflection is called the ***two-shock theory*** (Ben-Dor, 1992). The essential geometry for understanding two-shock theory is given in Figure 2.2. Steady self-similar flow is assumed, which is valid as long as real gas effects are not important. The frame of reference of this figure is fixed at the reflection point O, unlike that of Figure 2.1. Thus, the incident shock (I) and reflected shock (R) are stationary, while the gas state 0 has particle velocity with magnitude equal to the projection of the incident shock velocity in the incident angle. All shocks are assumed to be planar, not curved. Then, the planar oblique shock relations can be used to determine the final state across the incident shock. This state serves as the entry state for the reflected shock (R). The final state behind the reflected shock is labeled state 2. The flow beginning with entry into the incident shock and ending behind the reflected shock is suggested by the vectors and associated angles in Figure 2.2.

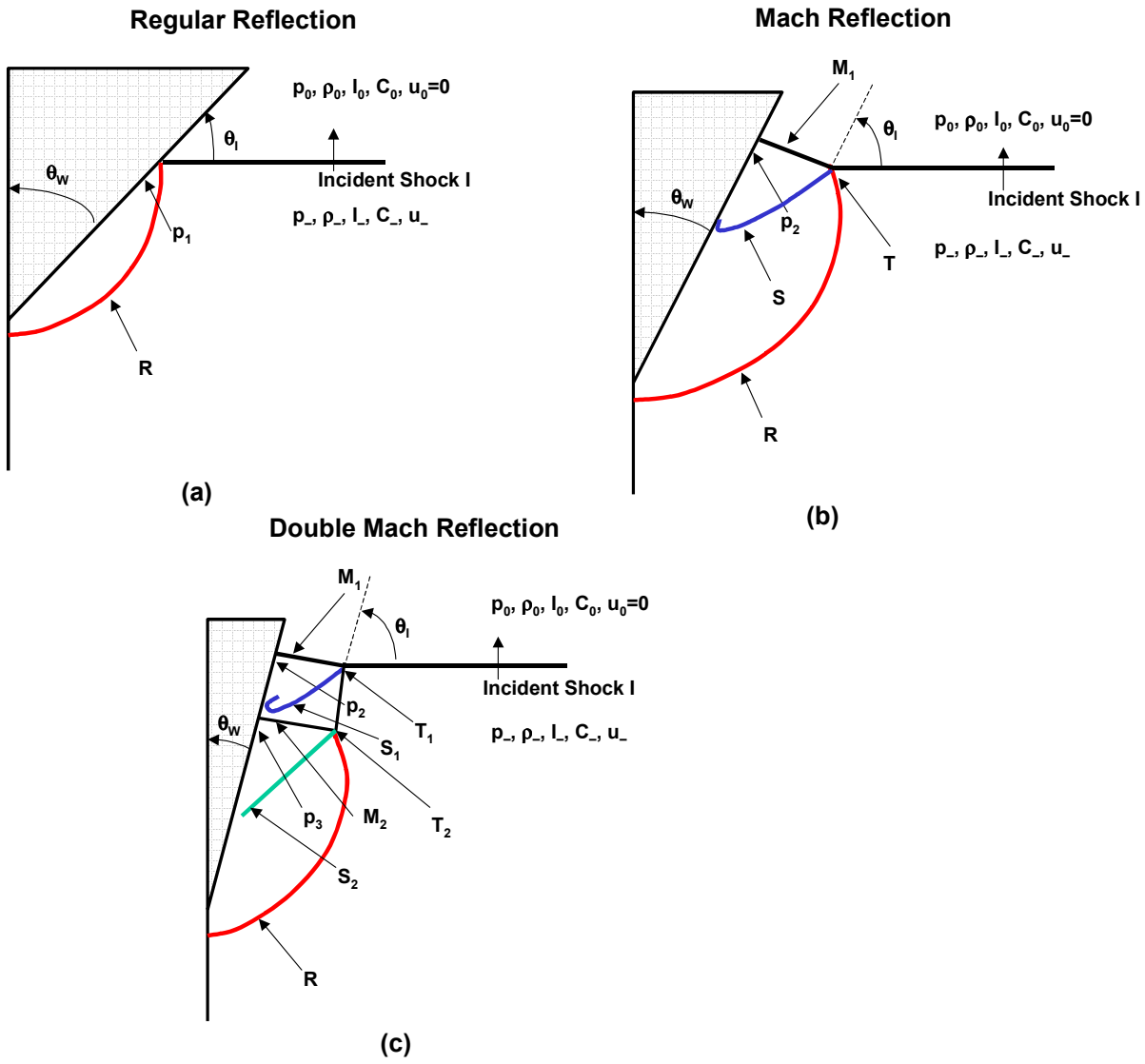

Figure 2.1 Schematics of possible shock reflection structures: (a) regular reflection; (b) single Mach reflection; and (c) double Mach reflection. This figure is redrawn from Sandoval (1987) with the same orientation as the ALEGRA calculations summarized in this document.

Because of planarity of the shocks and the steady state flow assumption, the oblique shock relations can be used to determine the final state 2 behind the reflected shock R. These equations are given by Ben-Dor (1992) and we repeat them here for reference:

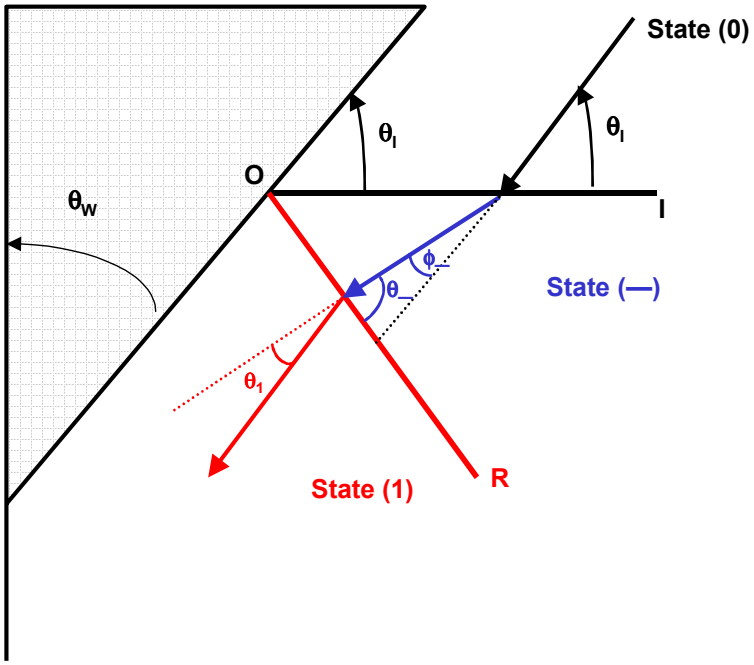

Figure 2.2 Geometry of the two-shock theory for regular shock reflection.

Oblique shock relations across the incident shock wave (I):

$$
\begin{aligned}
&\text{Mass:} && \rho_0 u_0 \sin\theta_I = \rho_- u_- \sin(\theta_I - \phi_-) \\
&\text{Normal Momentum:} && p_0 + \rho_0 u_0^{\,2} \sin^2\theta_I = p_- + \rho_- u_-^{\,2} \sin^2(\theta_I - \phi_-) \\
&\text{Tangential Momentum:} && \rho_0 \tan\theta_I = \rho_- \tan(\theta_I - \phi_-) \\
&\text{Energy:} && h_0 + \frac{1}{2} u_0^{\,2} \sin^2\theta_I = h_- + \frac{1}{2} u_-^{\,2} \sin^2(\theta_I - \phi_-)
\end{aligned}
\qquad (2.3)
$$

Oblique shock relations across the reflected shock wave (R):

$$
\begin{aligned}
&\text{Mass:} && \rho_- u_- \sin\theta_- = \rho_1 u_1 \sin(\theta_- - \theta_1) \\
&\text{Normal Momentum:} && p_- + \rho_- u_-^{\,2} \sin^2\theta_- = p_1 + \rho_1 u_1^{\,2} \sin^2(\theta_- - \theta_1) \\
&\text{Tangential Momentum:} && \rho_- \tan\theta_- = \rho_2 \tan(\theta_- - \theta_1) \\
&\text{Energy:} && h_- + \frac{1}{2} u_-^{\,2} \sin^2\theta_- = h_1 + \frac{1}{2} u_1^{\,2} \sin^2(\theta_- - \theta_1)
\end{aligned}
\qquad (2.4)
$$

The quantity $h = \frac{\gamma}{\gamma - 1}\frac{P}{\rho}$ in equations (2.3) and (2.4) is the enthalpy.

For inviscid flows the gas velocity behind the reflected shock wave is parallel to the surface of the wedge, implying that $\phi_{-} = \theta_1$. Together with this constraint, equations (2.3) and (2.4) form nine equations for thirteen variables. Specification of the initial state 0 and the angle of incidence of the shock (or the wedge angle) is sufficient to completely determine the final reflected shock wave state 2, but not uniquely. As discussed by Ben-Dor, Henderson (1982) showed that these equations can be simplified to a sixth order polynomial for the pressure p_1 in the case of an ideal gas. Only four of the possible solutions can be rejected on physical grounds.

In this report we will compare calculations with measurements of the pressure p_1 in state (1) behind the reflected shock wave in various experiments. These measurements will be discussed in Section 3 below. The pressure in Figure 2.1(a) illustrates where this pressure is measured both experimentally and computationally – immediately behind the reflected shock on the surface of the reflecting wedge where the analysis suggested by Figure 2.2 is as close to correct as possible. The quantitative experimental data that we will compare with our calculations is the ***pressure ratio*** that is produced during the shock reflection process. For regular shock reflection this ratio is defined as

$$\boldsymbol{R}^{(1)} = \frac{\Delta p_r{}^{(1)}}{\Delta p_{inc}} = \frac{p_1 - p_0}{p_{-} - p_0} \tag{2.5}$$

There is additional structure inside the reflected shock wave (R) that we have not depicted in Figure 2.1(a) or Figure 2.2, such as the structure called the ***corner signal*** (Heilig and Reichenbach, 1984). The state variables spatially vary over the region enclosed by R in reality because of the net curvature of this shock wave. Transition criteria for the transition from RR to MR depend on this structure.

2.1.1.2 Mach Reflection

Mach Reflection (MR) is depicted in Figure 2.1(b) and Figure 2.3. The major feature that is new is the presence of the ***Mach stem*** M_1. This shock wave intersects the reflected shock wave and the incident shock wave at a common point called the ***triple point*** T_1. Another new feature indicated in Figures 2.1(b) and 2.3 is the presence of a slip line S_1, across which the tangential velocity of the gas discontinuously changes. The slip line potentially can roll up into a vortex at the reflection surface when real gas effects

(viscosity) are important. While two-shock theory describes RR, ***three-shock theory*** describes MR in an approximate fashion, as shown in Figure 2.3.

The three-shock theory consists of the equations (2.3) and (2.4), as well as a similar set of oblique shock relations for the Mach stem M_1:

Oblique shock relations across the Mach stem (M_1):

$$
\begin{aligned}
&\text{Mass:} && \rho_0 u_0 \sin\phi_0 = \rho_2 u_2 \sin(\phi_0 - \theta_2) \\
&\text{Normal Momentum:} && p_0 + \rho_0 {u_0}^2 \sin^2\phi_0 = p_2 + \rho_2 {u_2}^2 \sin^2(\phi_0 - \theta_2) \\
&\text{Tangential Momentum:} && \rho_0 \tan\phi_0 = \rho_2 \tan(\phi_0 - \theta_2) \\
&\text{Energy:} && h_0 + \frac{1}{2}{u_0}^2 \sin^2\phi_0 = h_2 + \frac{1}{2}{u_2}^2 \sin^2(\phi_0 - \theta_2)
\end{aligned}
\qquad (2.6)
$$

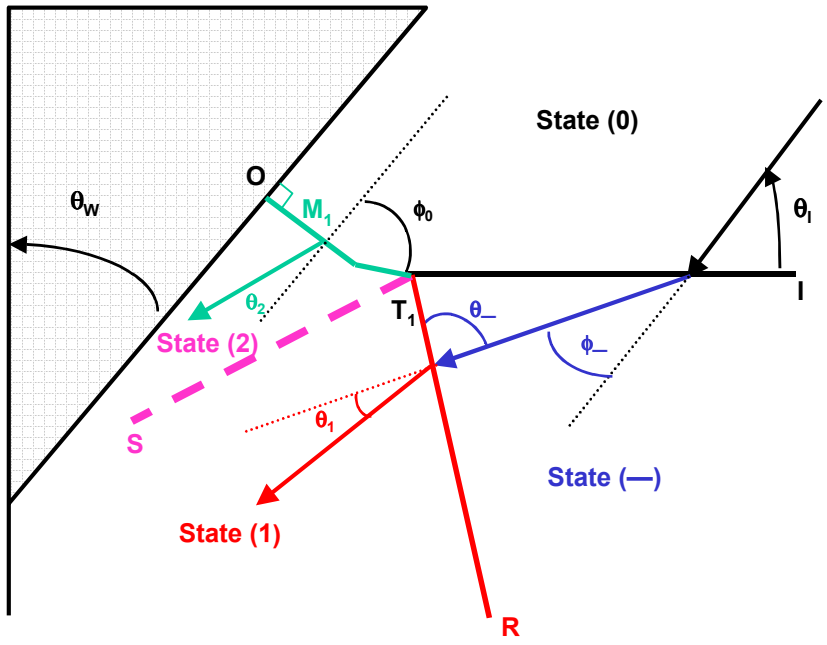

Figure 2.3 Geometry of the three-shock theory for Mach shock reflection.

The Mach stem is typically curved prior to its intersection with the triple point. We have depicted this as a single linear kink in the Mach stem itself in Figure 2.3. The key implication of Mach stem curvature in the three-shock theory is that the angle ϕ_0 is different than the incident angle θ_I. As an inviscid contact discontinuity, the slip line S_1 guarantees that $p_1 = p_2$ and that the gas flow is parallel on both sides of the slip, $\phi_- = \theta_1 + \theta_2$. These constraints, plus (2.3), (2.4), and (2.6), form fourteen equations for eighteen variables. Specification of the initial state plus the angle of incidence of the initial shock wave allows simplification of these equations to a tenth order polynomial for the pressure p_2. All but three of the roots of this polynomial can be discarded on physical grounds.

Transition from regular to Mach reflection is a key issue. Within the constraints of ideal gas flow this transition depends only on the ideal gas polytropic constant γ, the incident shock Mach number M and the incident shock angle θ_I. All of our computational results and comparisons with experimental data are expressed in terms of M and θ_I. The important feature to predict is the transition point for either fixed θ_I and varying M or vice versa. Such transition criteria are not trivial, as discussed in Ben-Dor and Glass (1979). Also, experiments typically show transition angles for fixed M that are greater by up to 2° – 3° than predicted by analytic transition criteria. The difference between experiment and theory is likely caused by non-equilibrium and viscous effects in real gases originating in the flow field near the finite tip of the wedge.

The pressure ratio for MR that we compare with experimental data is the same as for RR and given by:

$$\boldsymbol{R}^{(2)} = \frac{\Delta p_r^{(2)}}{\Delta p_{inc}} = \frac{p_2 - p_0}{p_- - p_0} \tag{2.7}$$

2.1.1.3 Double Mach Reflection

For either fixed θ_I and varying M or vice versa, the shock reflection process can be more complex than MR. This is shown in Figure 2.1(c) and is called double Mach reflection (DMR). This reflection is distinguished by two separate Mach stems, M_1 and M_2, two triple points T_1 and T_2, and two sliplines S_1 and S_2. Three-shock theory is insufficient to describe the shock reflection process in DMR.

There is also an intermediate regime of shock reflection between MR and DMR, called ***complex Mach reflection*** (CMR). This reflection regime results in a kinked reflected shock in the MR case, but without a fully developed second Mach stem. We do not consider CMR in this report.

We also note the speculation raised by Ben-Dor and Glass (1977) of having ***triple Mach reflection*** occur for sufficiently large Mach numbers as a transition from DMR. This regime of shock reflection has not been observed in the laboratory, although it might be seen computationally. We have not studied the possibility of triple Mach reflection in this work.

In DMR, there are two pressure ratios of interest that we will compare with experimental data. The first is calculated, as in equation (2.7), from the pressure immediately behind the first Mach stem. The other ratio is related to the pressure immediately behind the second Mach stem, p_3 in Figure 2.1(c). This second pressure ratio is defined by:

$$\boldsymbol{R}^{(3)} = \frac{\Delta p_r^{(3)}}{\Delta p_{inc}} = \frac{p_3 - p_0}{p_- - p_0} \tag{2.8}$$

2.1.2 Geometry, Grid, and Initial Conditions

The general computational geometry and initial conditions for our ALEGRA calculations are shown in Figure 2.4. All of the calculations reported here are performed using the Eulerian hydrodynamics capability of ALEGRA. The geometry is Cartesian x – y geometry. Thus, all regions are effectively of infinite depth into the page of any graphical view of the calculation. The Eulerian ALEGRA capability, as well as more general ALE capability, is described by Peery and Carroll (2000). The reader should note that Eulerian meshes used by ALEGRA are conformed to match the reflective boundary; the boundary of the reflective ramp depicted in Figure 2.1 is exactly geometrically represented in our calculations, not approximated by an inserted material boundary in an Eulerian mesh. A complete computational match to a specified shock reflection experiment must include the reflective material in the calculation, not simply a geometric representation of the boundary. However, it is standard practice in computational gas dynamics to not treat reflective boundaries as specific materials.

The most convenient and economical way to perform shock reflection calculations of the type discussed here is through the use of an Eulerian pressure boundary condition or an inflow boundary condition. This minimizes the amount of gas that must be in the problem, and thus minimizes the overall meshing requirements. However, neither of these boundary condition capabilities is currently supported in ALEGRA. Therefore, because we are not able to create a pressure or inflow boundary condition, we must simulate the incoming shock wave and the following gas as an initially moving material. That material must be fixed at the correct Hugoniot conditions for the corresponding steady shock wave we seek to generate. We achieve this by appending a block of mesh with gas at the appropriate conditions below the region that would only be required if inflow conditions were used. This secondary block of gas has an initial velocity corresponding to the correct Hugoniot material velocity state for the shock wave under

study. The initial data for this region in Figure 2.4 are generically labeled in the same way as in our discussion of the shock reflection process.

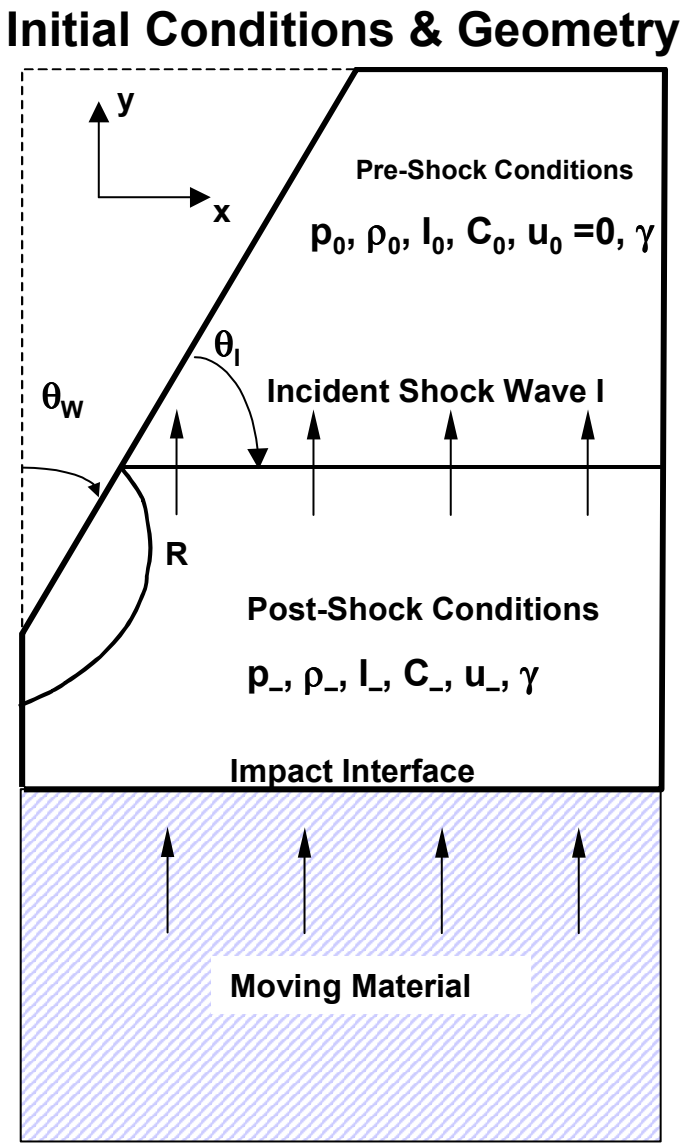

Figure 2.4 Sample of the initial data and geometry for ALEGRA Eulerian calculations of shock reflection from an oblique planar surface. The regions are effectively of infinite depth into the page because of the assumed Cartesian x – y geometry of these calculations.

This moving block of gas strikes a region of ambient gas, labeled as above with a subscript "0" in Figure 2.4. To insure steadiness of the incident shock wave the initial

region of moving gas must be long enough in the y – direction to prevent rarefactions from the bottom of the region to propagate into the shock reflection region. To summarize, the initial conditions, including block velocity, of the moving region of gas must be defined to generate a steady shock wave having the desired Mach number. The fact that we generate the shock wave of interest through means of an impact leads us to have concern about possible "start up" problems associated with the numerical approximation of the delta function acceleration at the interface between the ambient and the moving gas regions. Note that we have modeled the two different grid blocks with two different gases in our calculations. Thus, our calculations are multi-material calculations. Interface tracking is used to computationally maintain the boundary between the two distinct gases.

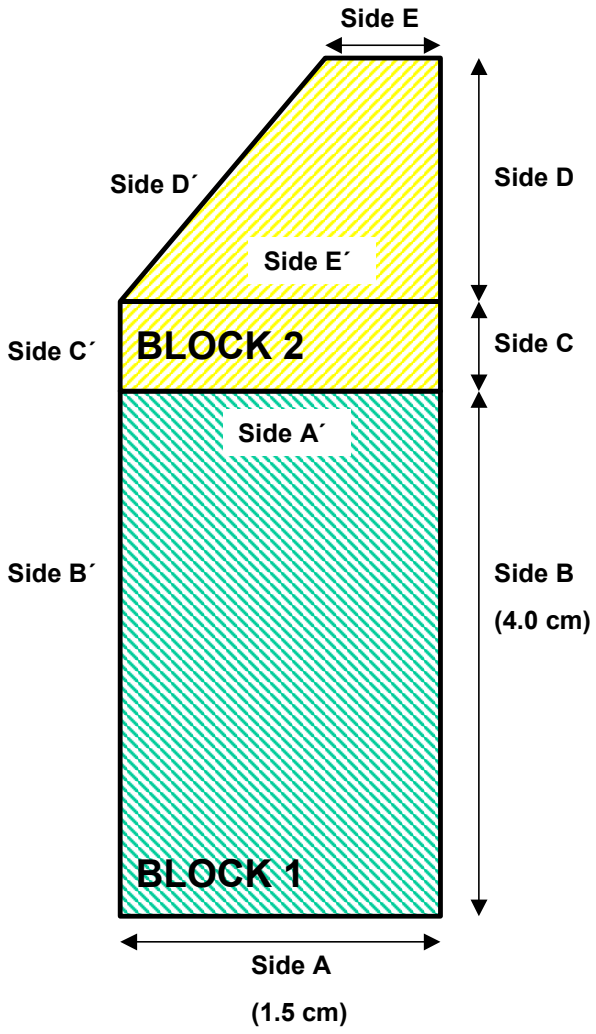

Figure 2.5 Schematic of the computational geometry and labeled sides for CUBIT meshing specifications.

Figure 2.5 shows the definitions of the computational blocks associated with the description of the initial conditions that we gave above. The initially moving block of gas that strikes the ambient gas is designated as "Block 1" while the ambient gas is "Block 2." Block 1 is always 4.0 cm long by 1.5 cm wide. Block 2 is the region of the ambient gas, including the wedge oblique reflection surface. The geometry of Block 2 is dependent upon the choice of wedge angle. We have designed the blocks to allow for a standoff distance between the impact plane of the two blocks and the beginning of the wedge. This is intended to allow any noise that might be produced by the impact generation of the incident shock wave to die away (as we will see) by the time the shock wave interacts with the wedge. As we pointed out above, once the initial conditions are chosen appropriately the type of shock reflection is completely determined by the angle of the wedge, the ideal gas constant, and the Mach number M of the shock wave.

In Figure 2.5 the basic meshing resolution is conveyed by information about the number of elements along the given labeled sides A through E. **Low** – resolution, **mid** – resolution, and **high** – resolution mesh schemes were chosen for the calculations that we discuss in this report. The meshing scheme is summarized in Table 2.1 in terms of this information. For side A, the low-resolution calculation had 75 elements, the mid-resolution calculation 150, and the high-resolution calculation 300. For side B, there were 33 elements in the low-resolution calculation, 66 and 264 elements in the mid- and high-resolution calculations, respectively. The elements were given a growth bias along side B in the direction away from the boundary with Block 2 in order to minimize computational effort by using elements that were as large as possible. It is our experience with Eulerian calculations that this increase in element size away from the critical shock generation and reflection regions should not influence the accuracy of the numerical simulation in those regions, even though it creates a varying grid with non-unit aspect ratio elements. We state again that the long initial column of gas in Block 1 is required so that a continual effective boundary condition at the wedge exists.

Table 2.1 Meshing Scheme.

Resolution	Number of Elements				
	Side A	Side B	Side C	Side D	Side E
Low	75	33	10	50	75
Medium	150	66	20	100	150
High	300	264	60	400	300

Block 2 had a maximum length of 1.2 cm and width of 1.5 cm (Figure 2.5 is not drawn to scale in the y – direction). As mentioned above, a rectangular region of elements, indicated by Side C in Figure 2.4, was appended to the region of the reflective wedge. For Side C, the low-resolution calculation had 10 elements, the mid-resolution had 20 elements, and the high-resolution calculation had 60 elements. Side A and Side E were defined in the meshing strategy to have equal numbers of elements, and this number held constant through the Block 1 – Block 2 boundary, suggested by the A′ and E′ notation in Figure 2.5. The same is true for the pairings Side B ↔ Side B′, Side C ↔ Side C′, Side D ↔ Side D′. In other words, the mesh we use in our calculations looks logically connected, even though it is a finite element mesh that could conceivably have been arbitrarily connected. There were 50 elements along side D in the low-resolution calculations, 100 in the middle-resolution calculation, and 400 in the high-resolution calculation.

We present an example of the meshing of Block 2 and the top of Block 1 in Fig 2.6. All meshing for our calculations was performed using the CUBIT meshing tool (CUBIT, 1994), Version 5.0. We give a sample of the type of CUBIT input deck used to generate the mesh for our calculations in Appendix A.

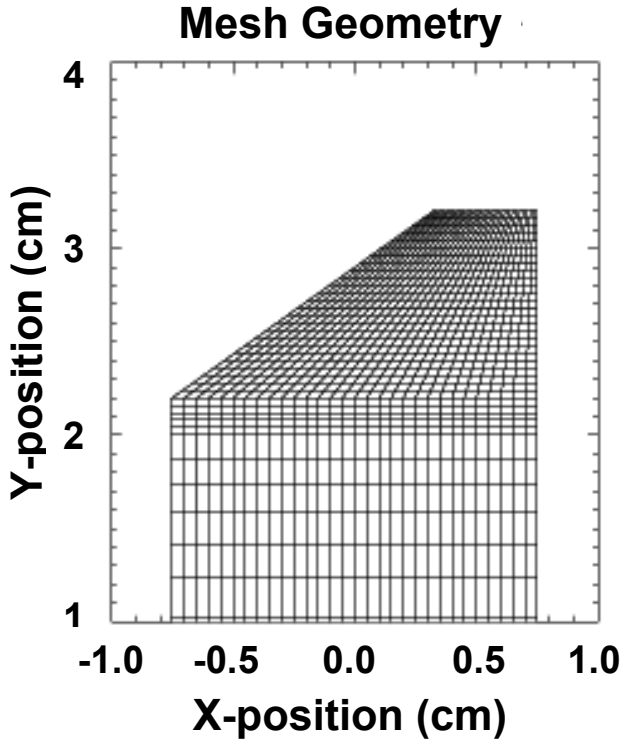

Figure 2.6 Example of the computational mesh in the region of shock formation, propagation, and reflection.

Detailed specification of the gas initial conditions in the two blocks for these calculations are given in Tables 2.2 and 2.3. The conditions for the ambient gas (state (–) in the wedge region) never change from calculation to calculation. These initial conditions specify a density of 1.0 g/cm^3, γ of 1.4, and a temperature of 300 Kelvin, as listed in Table 2.3. Two different initial conditions of the column of ideal gas impacting the stationary ideal gas around the wedge (Block 1) were run. These conditions are also noted in Table 2.2.

Table 2.2 Initial Conditions for Block 1.

Mach Number	Block 1 Velocity (cm/s)	Wedge Angle	Run ID	Ideal Gas Gamma	Sound Speed (cm/s)	Temperature (Kelvin)	Pressure (dynes/cm^2)	Density (g/cm^3)
1.37	0.53	40	1.37_40	1.4	0.53	369.562	1.45	1.64
		43	1.37_43					
		47	1.37_47					
		52	1.37_52					
		55	1.37_55					
3.36	2.55	40	3.36_40		2.55	937.835	9.29	4.16
		45	3.36_45					
		50	3.36_50					
		55	3.36_50					

Table 2.3 Initial Conditions for Block 2

Mach Number	Ideal Gas Gamma	Sound Speed (cm/s)	Temperature (Kelvin)	Pressure (dynes/cm^2)	Density (g/cc)
1.37	1.4	1.0	300	0.714	1.0
3.36					

All other variations of this problem involve changes in the wedge angle. Once again, depending on the wedge angle, gamma, and shock speed in Block 1, simple reflection,

Mach or a double Mach stem will form along the wedge (Figures 2.3). We have performed calculations over incident angles in the range of 30° to 50°.

The reader will observe that the specified initial conditions of the calculations, such as a sound speed of 1.0 cm/s and density of 1 g/cm^3, do not really match any realistic experimental conditions for gases in real shock tube facilities. We are mimicking the way that Sandoval (1987) performed these calculations. In the absence of known real gas effects, all of the phenomena are uniquely determined by the polytropic gas constant, the constant volume heat capacity, the incident angle, and the incident shock wave Mach number. This strategy will not work if dimensional quantitative experimental data, such as flowfield isopycnic contours or absolute pressure measurements, are reported. Also, if real gas effects are important then flowfield temperatures are also important and it is important to match true experimental conditions so as to most accurately match the actual experimental temperatures.

2.1.3 Example Calculations

In this section we will illustrate ALEGRA results for each of the shock reflection regimes of interest. These results show snapshots of the calculated flow fields at a calculation time of 0.7 seconds as well as a plot of the calculated pressure field along the surface of the reflecting wedge at the same time. These results demonstrate the ability of ALEGRA to calculate shock wave reflections of all three types. The assessment of the accuracy of these results is given in Section 3.

2.1.3.1 Regular Shock Reflection

Figure 2.7 illustrates the case of a regular shock wave reflection problem. The calculation for this example had a specified Mach number of 1.37 and a incident angle of 35 degrees (calculation 1.37_55 in Table 2.2). Both pressure and density are plotted along with their contours at the calculation time of 0.7 seconds. (All contours in this report are unlabeled. The intent is to visualize the nature of the flow field in the important regions, not to quantify the particular field variable selected for contouring.) In Figure 2.8, the gradient of the pressure and density are plotted at the same calculation time. These plots are especially useful to highlight the incident and reflected shock discontinuities in the calculation. The attachment point O on the wedge can be seen very clearly. These plots were produce using the Ensight7 (Computational Engineering International, 2001) visualization package. The arrows shown in Figures 2.7 and 2.8 show the location of the shock front in a plot along the surface of the wedge, which is separately plotted below.

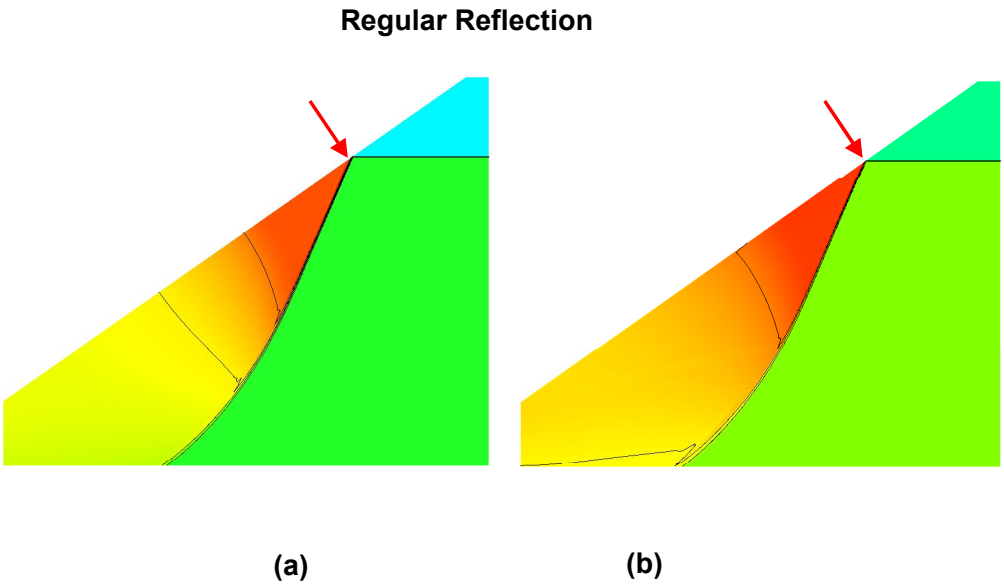

Figure 2.7 Sample (a) pressure and (b) density plot with contours (drawn but not labled) for regular shock reflection calculation with a Mach number of 1.37 and incident angle of 35 degrees at a calculation time of 0.7 s. The arrow correlates this figure with the plot in Figure 2.9.

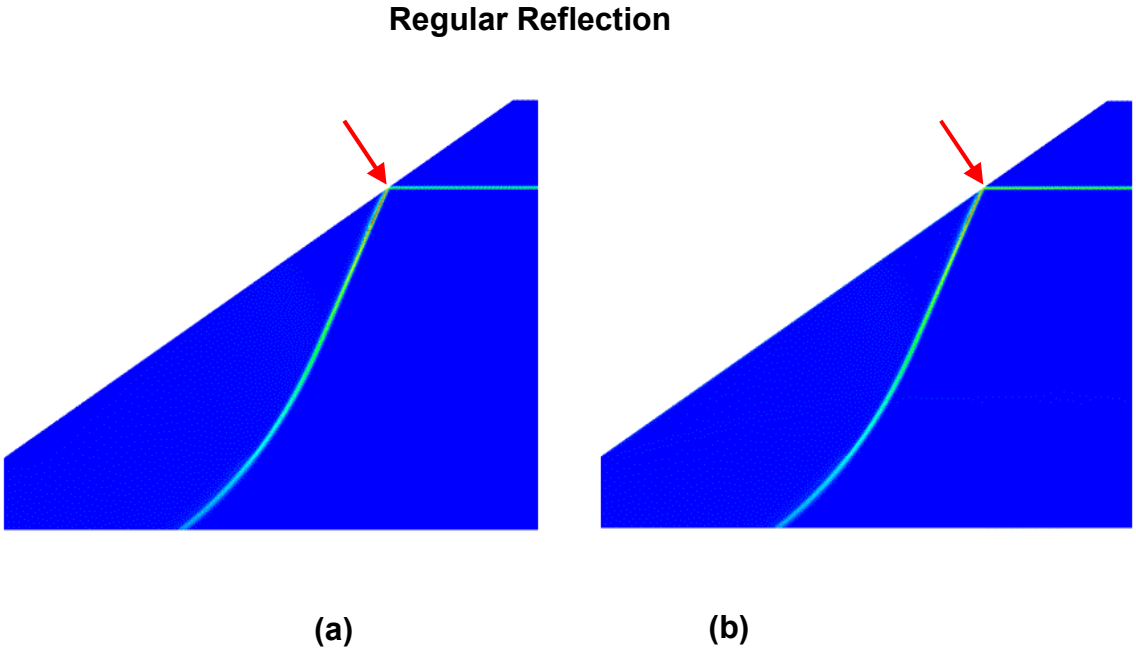

Figure 2.8 Sample gradient of the (a) pressure and (b) density plot with contours for regular shock reflection calculation with a Mach number of 1.37 and incident angle of 35 degrees at 0.7 s. The arrow correlates this figure with the plot in Figure 2.9.

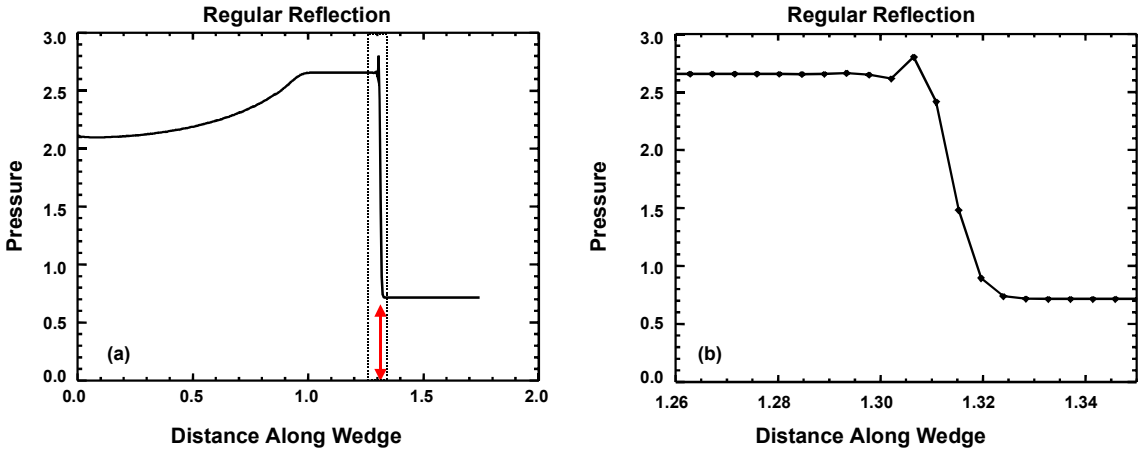

Figure 2.9 (a) Pressure plot with distance measured along the face of the wedge in the flow direction for the regular shock reflection calculation with a Mach number of 1.37 and incident angle of 35 degrees. (b) Zoom of the plot over the region indicated by the dotted rectangle in plot (a).

In Figure 2.9 (a), the pressure plot just mentioned is plotted at the same calculation time of 0.7 seconds. This is a representation of the pressure along a line of elements just off the surface of the wedge for this regular reflection calculation. The element centered pressure data are extracted from a plot tool available in Ensight7 and plotted using the IDL visualization tool (Research Systems, 1998). Figure 2.9 (b) is a magnification of the region in the vicinity of the shock front that clarifies the fine structure around the shock. The locations of the elements from which the data were extracted are marked in this plot by the discrete dots. This plot makes it apparent that the artificial viscosity in this calculation has smeared the shock front over approximately four zones. The shock is also not completely monotonic, for an overshoot and post shock oscillation is clearly visible over two or three elements following the shock wave peak pressure. As we will discuss later, the presence of post shock oscillations complicates the task of data comparison of the calculations with the experimental data.

2.1.3.2 Mach Shock Reflection

Figure 2.10 shows an example of a single Mach reflection. This calculation used an incident angle of 50 degrees (wedge angle of 40 degrees) and a Mach number of 1.37 (calculation 1.37_40 in Table 2.2). Both pressure and density are plotted along with their contours at the calculation time of 0.7 seconds as for the regular reflection calculation. In Figure 2.11, the gradient of the pressure and density for this calculation are plotted and clearly show the structures discussed in Figure 2.3, including the incident, reflected, and Mach shock waves, as well as the triple point. The slip line will not be visible for this calculation from plots of these variables. As in the case of the regular reflection

discussed above, the arrows in Figures 2.10 and 2.11 show the location of the incident shock front for correlation with a plot selected along the face of the wedge.

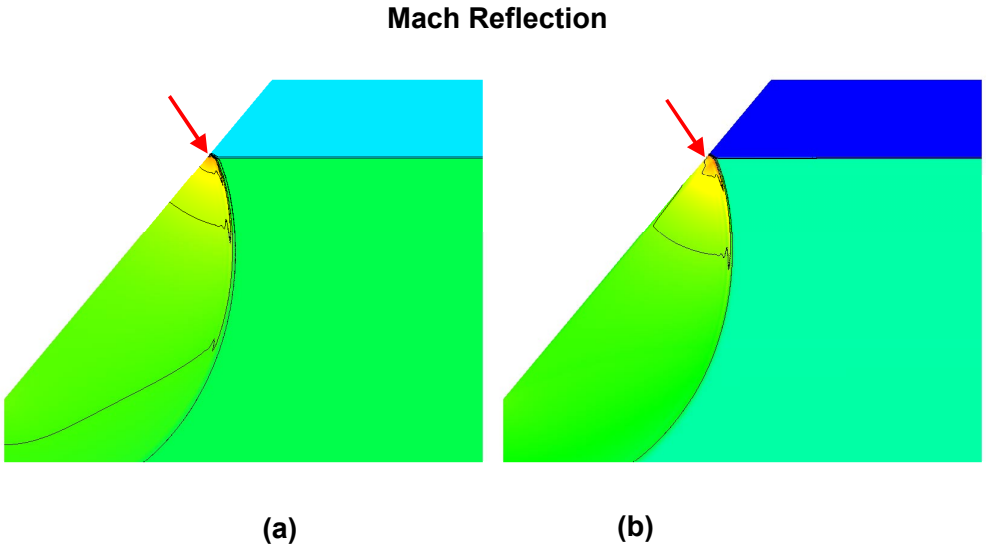

Figure 2.10 Sample (a) pressure and (b) density plot with contours for Mach shock reflection calculation with a Mach number of 1.37 and incident angle of 50 degrees at 0.7 s. The arrow correlates this figure with the plot in Figure 2.12.

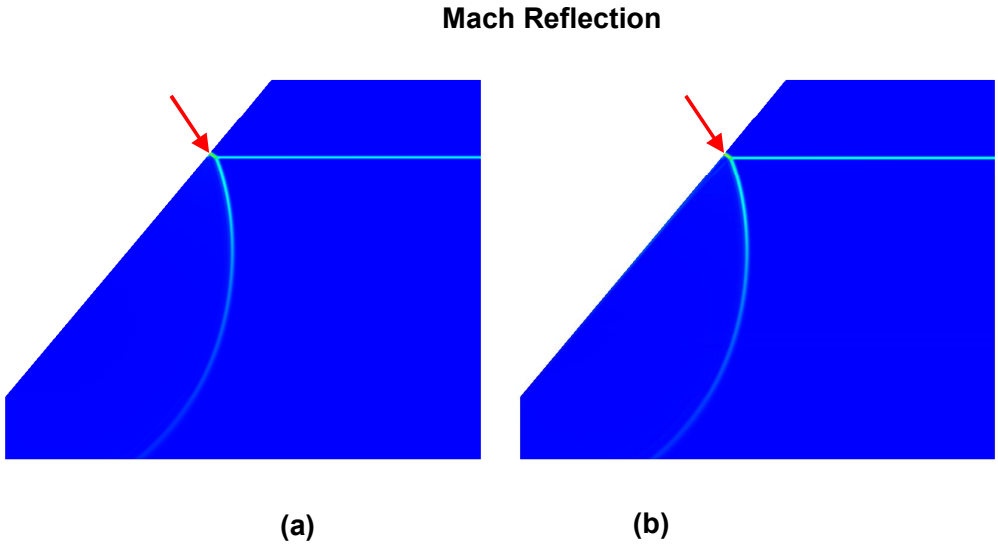

Figure 2.11 Sample gradient of the (a) pressure and (b) density plot with contours for Mach shock reflection calculation with a Mach number of 1.37 and incident angle of 50 degrees at 0.7 s. The arrow correlates this figure with the plot in Figure 2.12.

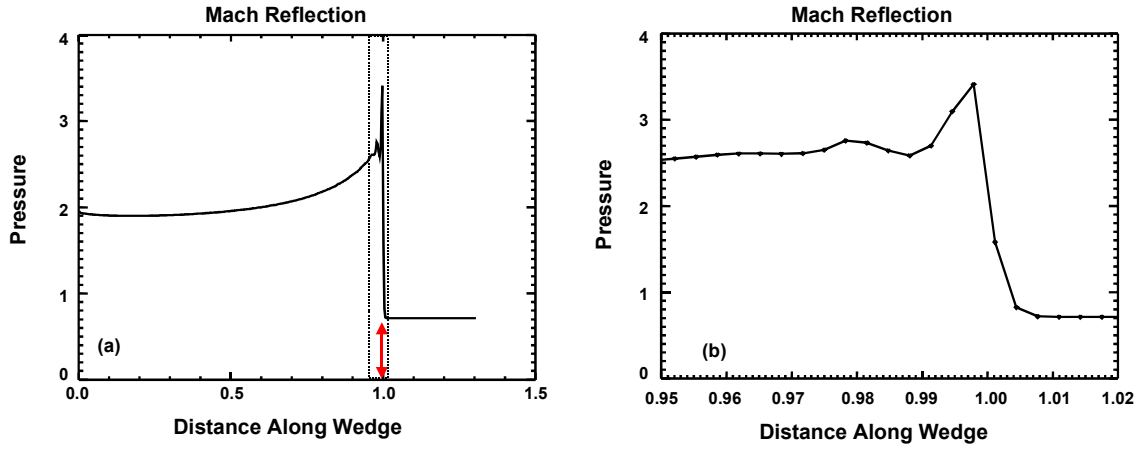

Figure 2.12 (a) Pressure plot with distance measured along the face of the wedge in the flow direction for the Mach shock reflection calculation with a Mach number of 1.37 and incident angle of 50 degrees. (b) Zoom of the plot over the region indicated by the dotted rectangle in plot (a).

Figure 2.12 (a) shows the pressure plot corresponding to the one we discussed for the regular reflection calculation at the calculation time of 0.7 seconds. Figure 2.12 (b) shows a magnification of the region in the vicinity of the shock front. This plot helps clarify more precisely the flow region behind the Mach stem, although there is still some question as to which is the correct pressure to use for comparison with experimental data due to the even more pronounced overshoot and post-shock oscillation in this calculation.

2.1.3.3 Double Mach Shock Reflection

Figure 2.13 is an example of a double Mach reflection. This calculation used an incident angle of 45 degrees and Mach number of 3.36 (calculation 3.36_45 in Table 2.2). Both pressure and density are plotted with their contours. A magnified view of the double Mach stem is shown in Figure 2.14. In the density plot, a slip line can be distinctly observed. In Figure 2.15, the gradient of the pressure and density are plotted. These plots highlight the shock discontinuities and substructure of the Mach region. The slip line is also clearly visible in the density gradient plot. The arrows in these plots have the same significance as in our discussion of the regular and single Mach reflection calculations above.

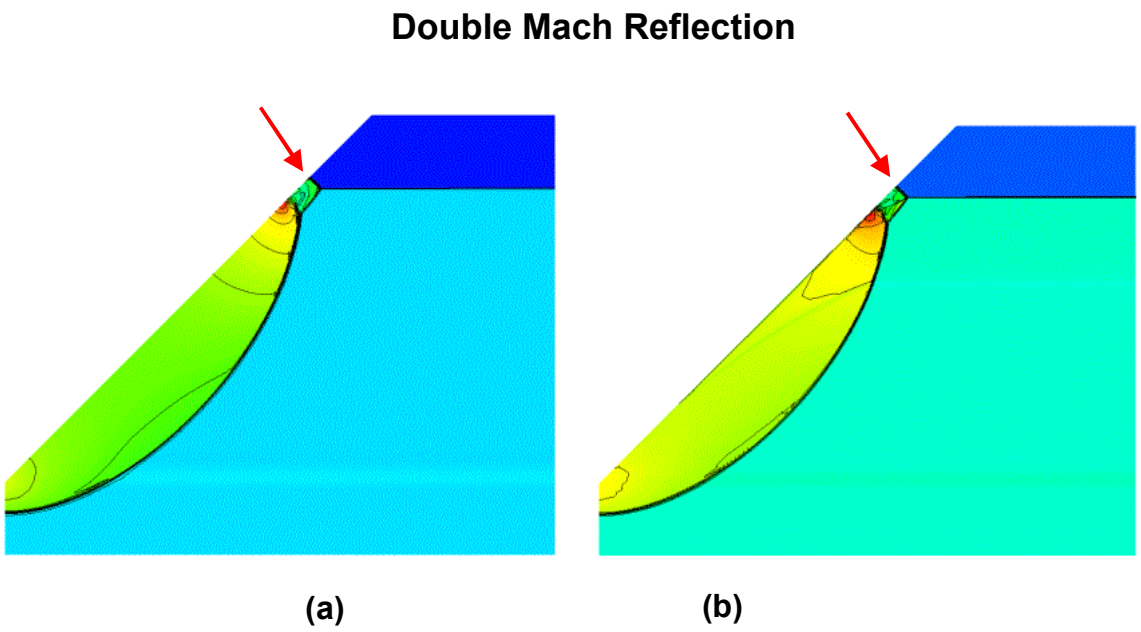

Figure 2.13 Sample (a) pressure and (b) density plot with contours for double Mach shock reflection calculation with a Mach number of 3.36 and incident angle of 45 degrees at 0.7 s. The arrow correlates this figure with the plot in Figure 2.16.

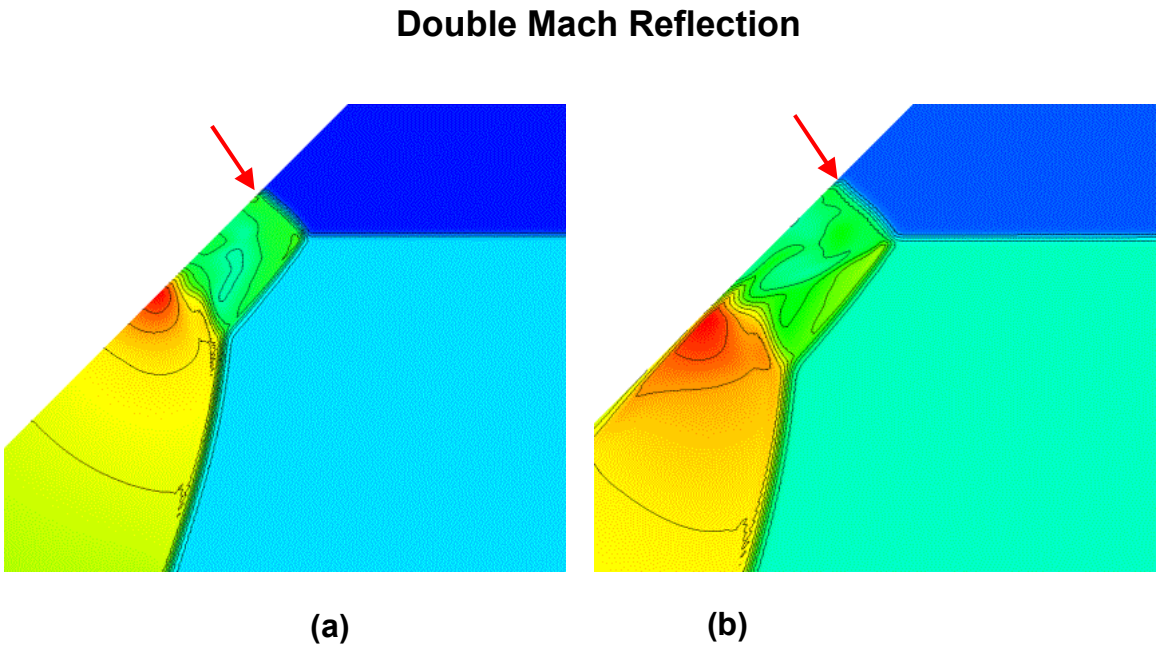

Figure 2.14 Enlarged view of sample (a) pressure and (b) density plot with contours for the double Mach shock reflection calculation with a Mach number of 3.36 and incident angle of 45 degrees at 0.7 s. The arrow correlates this figure with the plot in Figure 2.16.

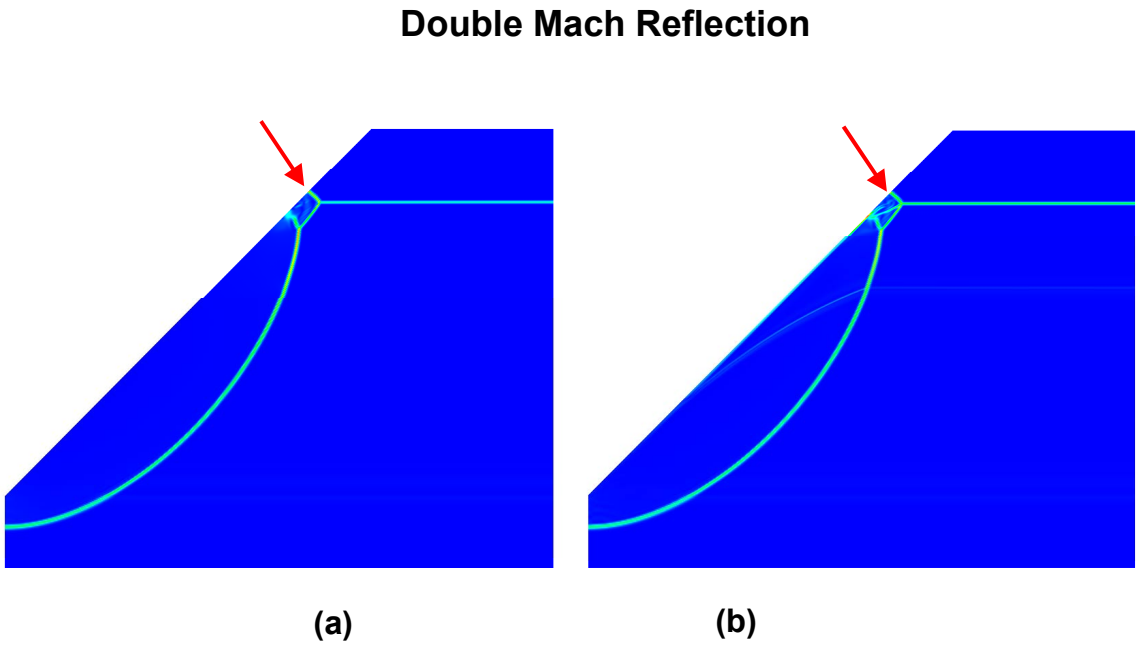

Figure 2.15 Sample gradient of the (a) pressure and (b) density plot with contours for double Mach shock reflection calculation with a Mach number of 3.36 and incident angle of 45 degrees at 0.7 s. The arrow correlates this figure with the plot in Figure 2.16.

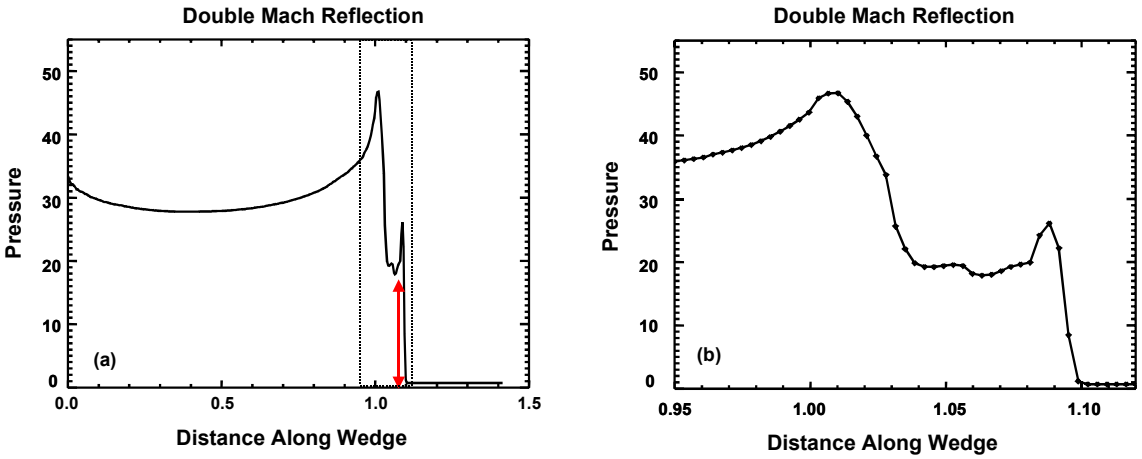

Figure 2.16 (a) Pressure plot with distance measured along the face of the wedge in the flow direction for the double Mach shock reflection calculation with a Mach number of 3.36 and incident angle of 45 degrees. (b) Zoom of the plot over the region indicated by the dotted rectangle in plot (a).

The pressure plot along the wedge at the calculation time of 0.7 seconds is presented in Figure 2.16 for this double Mach reflection calculation. The smearing due to artificial viscosity is clearly visible, especially in the region of the second Mach stem, as well as additional structure due to post-shock oscillation in the first Mach stem. Oscillatory artifacts, however, are less apparent in the second Mach stem.

Figure 2.17 presents another example of the calculation of a double Mach reflection. This calculation used a wedge with an incident angle of 50 degrees and a Mach number of 3.36 (calculation 3.36_40 in Table 2.2). In this case, the double Mach stem is even more pronounced than for the 45 degree calculation. Density is plotted along with its contours in Figure 2.17 (a). Figure 2.17 (b) is an enlarged view of Figure 2.17 (a). Note the very visible slip line that can be observed in this case. In Figure 2.18 (a), the gradient of the density is plotted, once again highlighting the shock substructure. An enlarged view is plotted in Figure 2.18 (b). The obvious heterogeneity of the flow field behind the first Mach stem illustrates the difficulty one would face in accurately extending three shock theory to some kind of "four shock theory" to approximate the pressure behind the second Mach stem.

In Figure 2.19 we illustrate the transition of the plots for pressure along the surface of the wedge as a function of incident angle for both Mach numbers of 1.37 and 3.36.

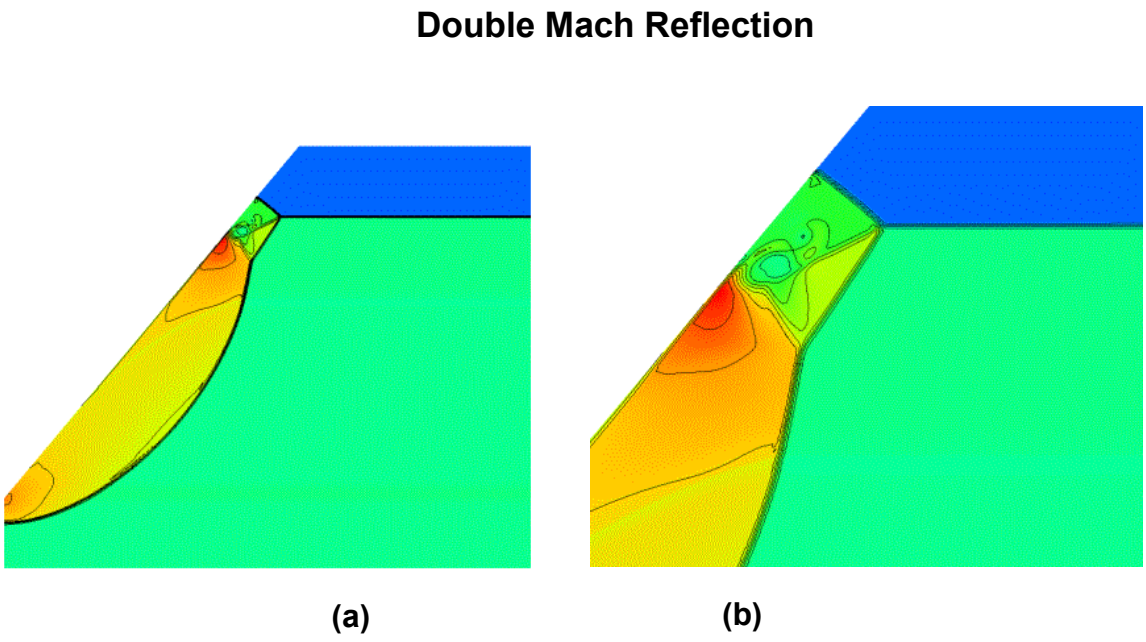

Figure 2.17 Sample (a) pressure and (b) density plot with contours for double Mach shock reflection calculation with a Mach number of 3.36 and incident angle of 50 degrees.

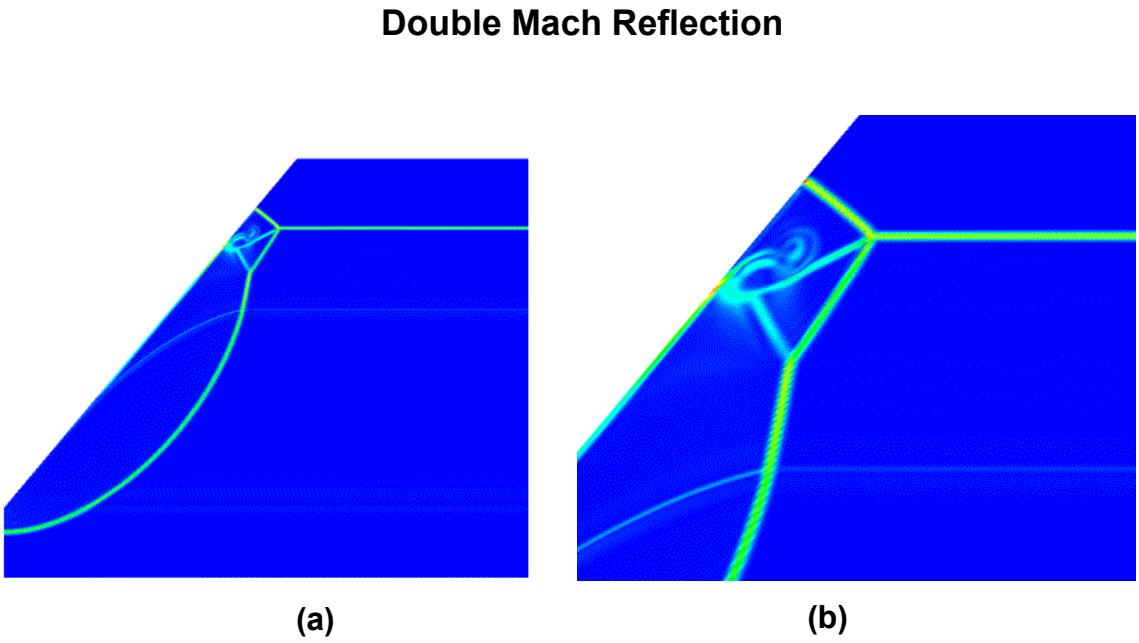

Figure 2.18 Sample gradient of the (a) pressure and (b) density plot with contours for double Mach shock reflection calculation with a Mach number of 3.36 and incident angle of 50 degrees.

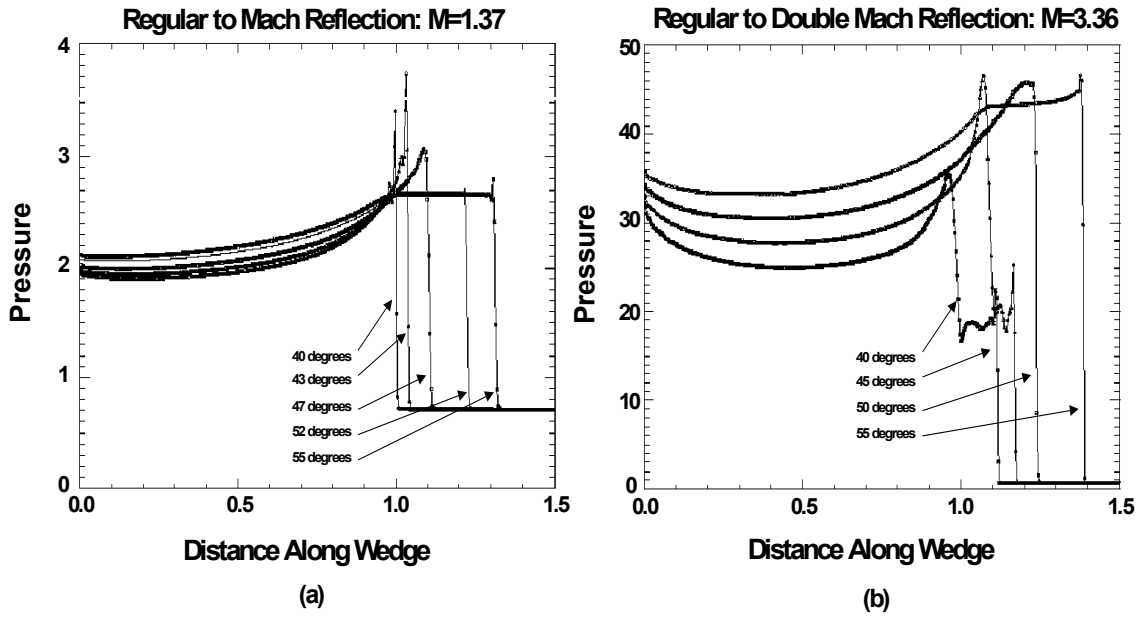

Figure 2.19 Pressure – distance plots versus wedge angle for (a) M=1.37 and (b) M=3.36 at 0.7 seconds calculation time.

Figure 2.19 quantitatively illustrates the computed nature of the regular to Mach and regular to double Mach shock reflections in terms of the pressure plots along the reflecting wedge. These plots are overlaid as a function of wedge angle at the same calculation times. This figure illustrates the numerical overshoot of the pressure in the reflected shocks and first Mach stem, as well as the poor quality of the numerical detail in the double Mach region for the 40-degree case. This is probably a numerical resolution issue.

As we stated before, the steadiness of the shock front through block 2 is a computational concern because of the manner in which we must initiate the shock wave in our ALEGRA calculations. The shock propagation into Block 2 (Fig 2.5) must be steady to insure computational consistency and accuracy for comparing with experimental data. Therefore, in Figure 2.20 (a) and (b) the pressure and density along the row of elements just below the Block 1 – Block 2 boundary are plotted versus time for the 3.36 Mach calculation with a 45-degree wedge angle. These plots show the presence of a transient originating in the impact of Block 1 upon Block 2 in both the pressure and density. The transients quickly vanish, by approximately a calculation time of 0.04 seconds, and a constant effective incoming flow boundary condition is subsequently observed. This transient is further quantified by the plots in Figure 2.20 (c) and (d). These plots show the percent relative error of the transient, which is calculated using the formula

$$\text{Error} = \left(\frac{X_i - X_f(t)}{X_i} \right) \times 100 \qquad (2.9)$$

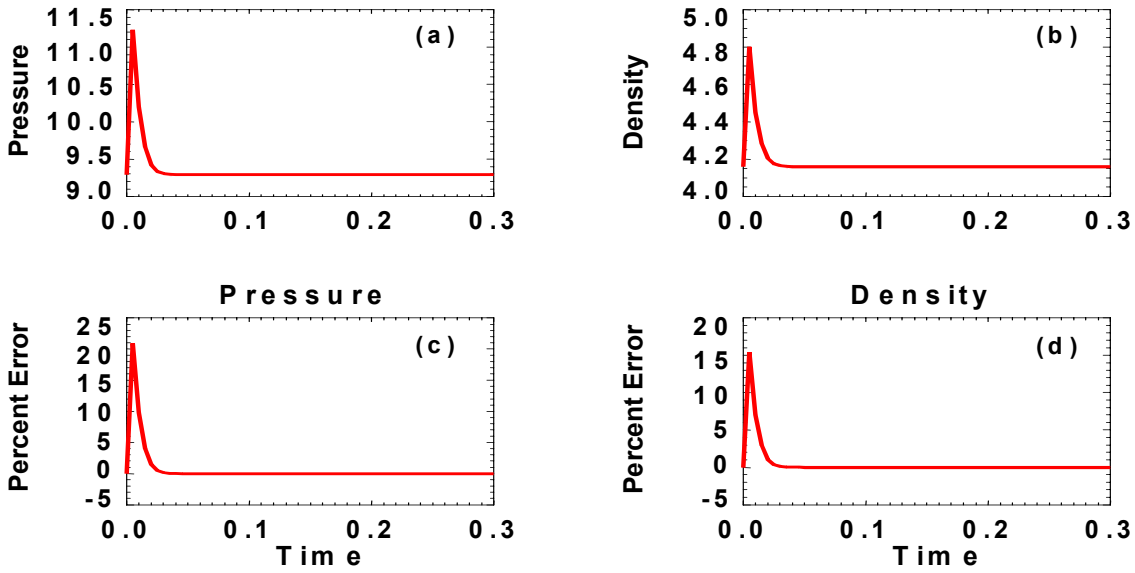

Figure 2.20 Top row: Plot of (a) pressure and (b) density along the row of cells just below the boundary between Block 1 and 2 (Fig 2.3) versus time. Bottom row: the percent relative error in the (c) pressure and (d) density, when compared to the initial condition.

In Eq (2.9), $X = p$ or ρ; the index "i" denotes the initial value of the quantity for Block 1; and the index "f" indicates the corresponding time dependent value after the calculation has been started. In an ideal steady state through this line of cells, this error would be identically zero to machine precision. The transient is so fast, over an order of magnitude faster than the data gathering calculation time of 0.7 seconds, that it has no influence on the reflected shock. The transient has completed before the shock wave initially reflects off the wedge, for example. This explains why we designed Block 1 to stand off a finite distance from the apex of the wedge.

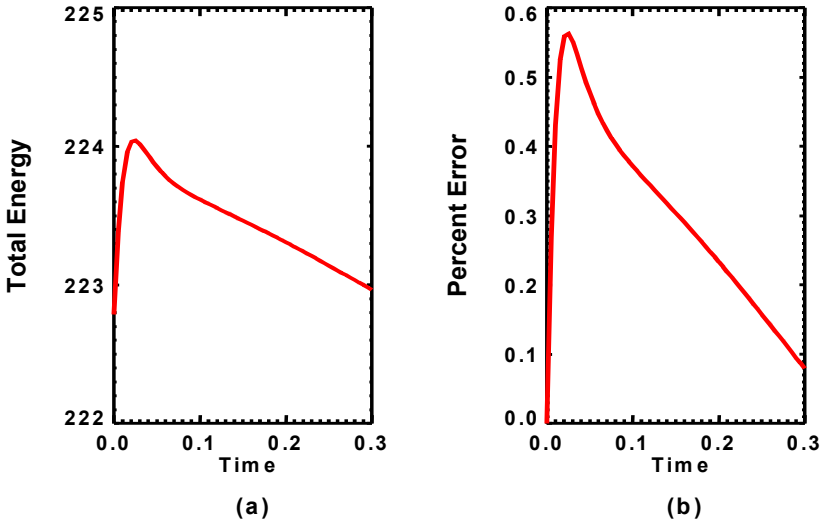

Figure 2.21 Plot of total energy vs time in the Mach 3.36 calculation with a wedge angle of 45 degrees (a) and the percent error in the total energy when compared to the initial conditions.

Another useful method that allows us to confirm the lack of important influence of the start up transient in these calculations is to consider energy conservation. We have done this in Figure 2.21. Figure 2.21 (a) shows total energy versus time for a calculation with a Mach number of 3.36 and a wedge angle of 45 degrees. Figure 2.21 (b) plots the percent relative error, using the same equation (2.9) with X chosen as total energy. In a perfect computation, there would be no gain or loss of energy. From the plots in Figure 2.21 we see that some energy is gained during the transient, approximately 0.5% relative error. This is not a significant amount, and has drifted to approximately 0.1% by the calculation time of 0.3 seconds. A small energy conservation error is expected in ALEGRA Eulerian calculations because of the algorithmic decisions implemented regarding advection of total, kinetic, and internal energy.

We present one final method for testing the steadiness of the generated shock wave in our calculations. This is an overlay of vertical plots of pressure through the calculation geometry at various calculation times. The location of the selected plot is shown in Figure 2.22 (a). This is chosen so that the reflection point O on the wedge does not intersect the lineout over the range of times selected. The resulting pressure versus distance lineout for the calculation times of 0.2, 0.4, and 0.7 seconds are shown in Figure 2.22 (b). These plots demonstrate how steady the impact generated shock wave is as it propagates through Block 2. Based on these results we do not believe that transients associated with the initial collision of Block 1 gas with Block 2 gas influence the shock reflection process. Therefore, we do not believe that such transients need to be accounted for in our comparisons with experimental data.

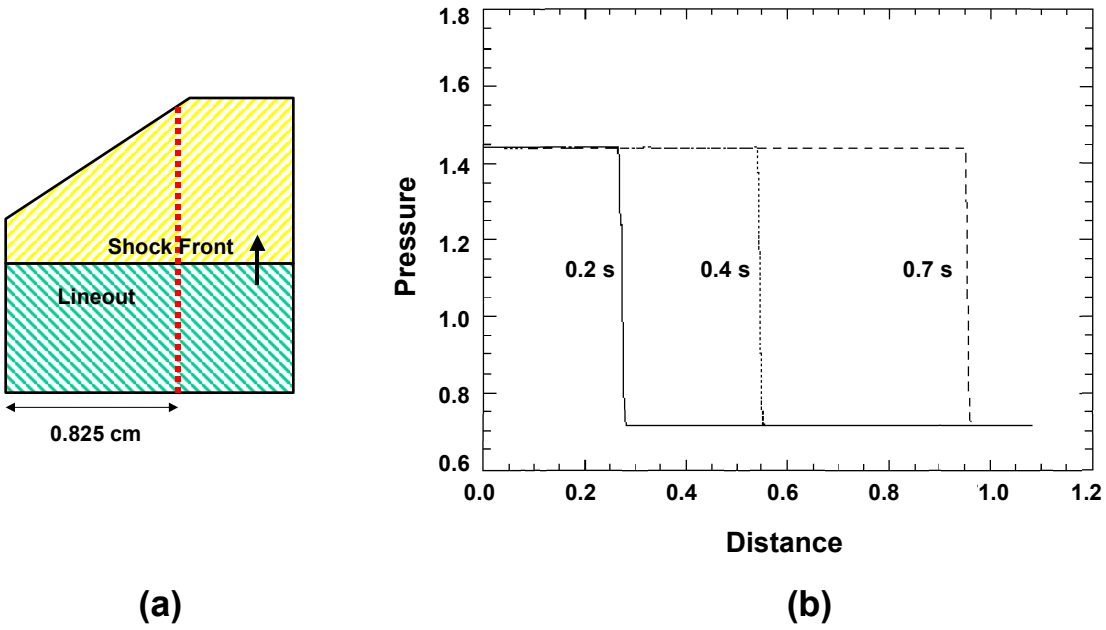

Figure 2.22 (a) Schematic of where the plot was taken for the pressure versus distance plot and (b) the pressure vs distance plot at three different times.

3. Comparison With Experimental Data

3.1 Summary of Experimental Data

The data that we use to evaluate the accuracy of ALEGRA shock reflection calculations are presented in Sandoval's original Los Alamos report (1987) and originate in the work of Heilig and Reichenbach (1984). We will first review these data.

The experimental configuration reported by Heilig and Reichenbach was an air/air shock tube. For the conditions of the experiments, which were conducted over the range of Mach number of 1.26 to 3.36, using a $\gamma = 1.4$ ideal gas model as the equation of state of air is expected to be accurate, except for certain caveats. The resulting density compression ratios achieved by the measured shock waves that correspond to this range of Mach numbers are approximately 1.4 to 4.2. The upper limit of this range of compression ratios is considered to be representative of the strong shock regime, hence of relevance to validation for ALEGRA HEDP applications. (A peak compression ratio of 4.2 is still far less than the compression ratios that occur in real Z-pinch implosions and fusion capsule implosions, of course.) Additional information on the experimental configuration is discussed in Heilig and Reichenbach, although it is implicitly clear that some familiarity with the design and performance of such shock tubes is assumed for the reader of that paper.

Heilig and Reichenbach gather two classes of data in their paper. First, they measured schlieren images of shock reflections in all three reflection regimes (RR, MR, and DMR) of interest in our work. From the schlieren images, both qualitative characteristics (RR versus MR versus DMR, for example) as well as quantitative characteristics (shock curvature, or intersection angles at triple points, for example) can be evaluated. The schlieren images also provided complementary evaluation of pressures from observed shock speeds in the images by using the Hugoniot relations (2.2) and the known Mach number and initial state of the gas. These images could be qualitatively compared with our calculations, but we will not do that in this report.

Second, Kistler pressure transducers were placed on the surface of the wedges used in these experiments. These gauges recorded time-resolved pressure data. The peak pressure data we record from our computational plots along the surface of the wedge are the computational analogs of the peak pressures recorded by the Kistler gauges in the experiments. If we chose to exactly simulate the experimental shock tube, including the exact positions of the pressure gauges, we could present time-dependent fixed location

pressure data that would be exact analogs of the experimental Kistler gauge data. Heilig and Reichenbach's paper, however, does not present detailed information about experimental dimensions, gauge positions, and other required information. In any event, direct simulation of a shock tube experiment is not in the scope of our current computational work.

The experimental gauge data are reduced to form the pressure ratios we defined in Section 2. These data for the two Mach numbers 1.37 and 3.36 that we are interested in are plotted in Figures 3.1 and 3.2. We interpret error bars in these figures to represent diagnostic fidelity. While the schlieren data can be used to calibrate and cross-validate the time-resolved gauge data there are timing errors in the schlieren images that introduce resolution problems (these timing error are not discussed in absolute terms by Heilig and Reichenbach). At the same time, the pressure transducers provide an area-averaged response to the passage of the shock wave because of their finite areas and finite temporal response. These combined considerations of diagnostic fidelity are apparently the source of the error bars associated with the experimental data in Figures 3.1 and 3.2.

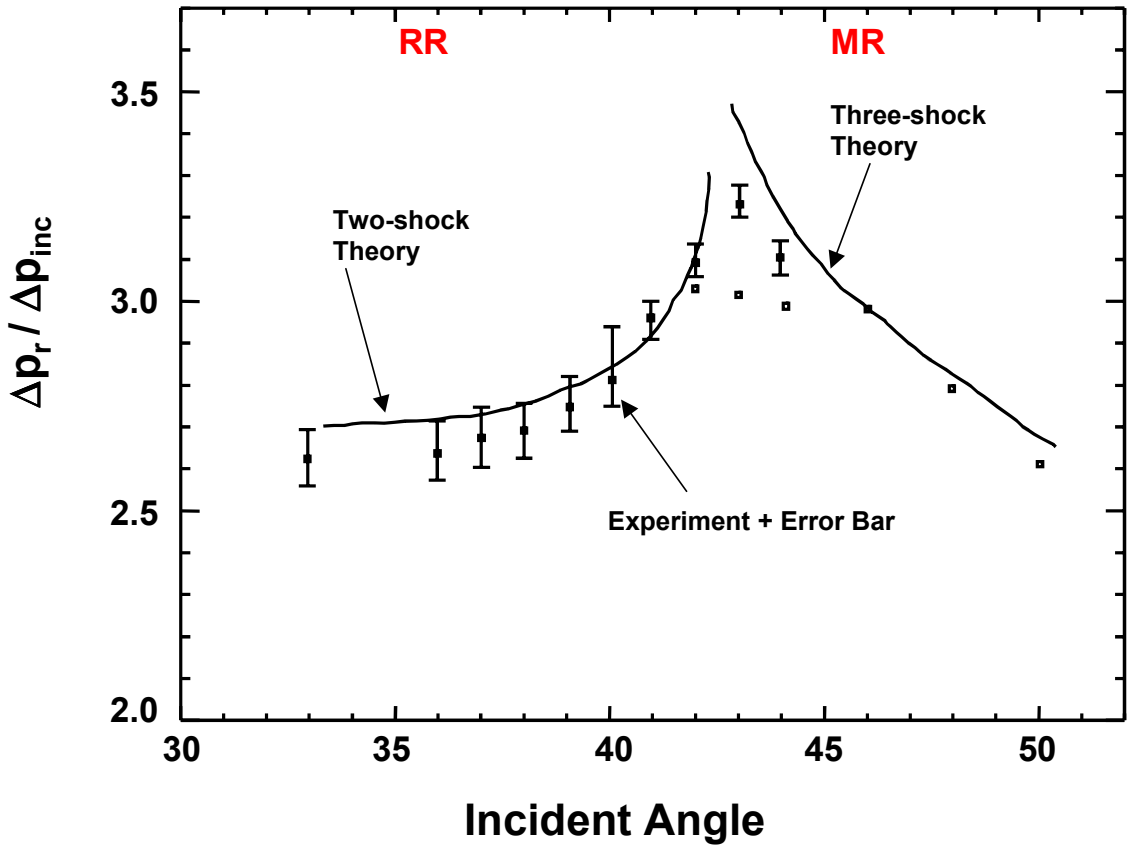

Figure 3.1 Plot of experimental data and analytic theory for Mach 1.37 experiments. This figure is a reproduction of a figure in Sandoval (1987) and has multiple sets of experimental data included. This is why there are multiple experimental data for incident angles between 40 and 45 degrees.

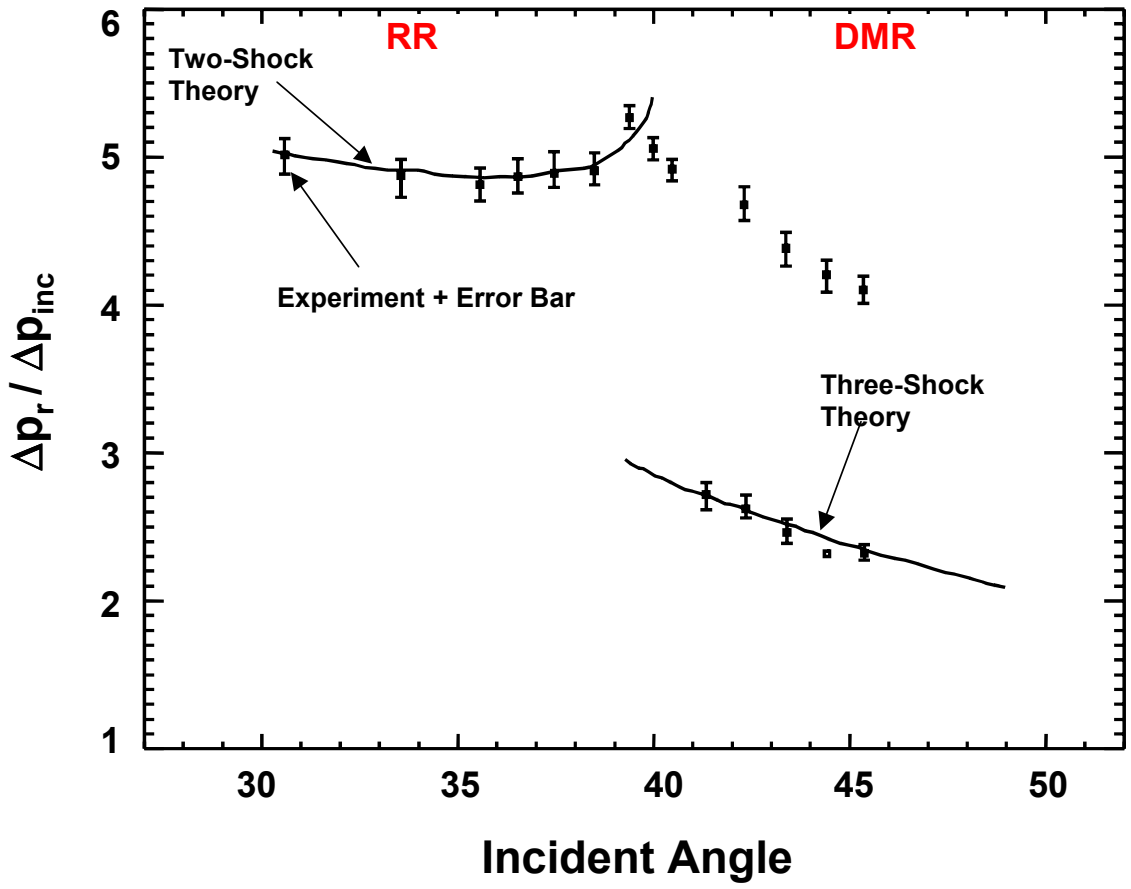

Figure 3.2 Plot of experimental data and analytic solution for Mach 3.36 calculation. As in Figure 3.1 this figure is a reproduction of an identical figure in Sandoval (1987). There are multiple sets of experimental data included. The range of incidence angles greater than 40 degrees has multiple pressure data corresponding to the presence of two Mach stems in the experiments.

In Figures 3.1 and 3.2 the left branch of the analytic curves is given by two-shock theory, while the right branch (lower right branch for the DMR experiments) is given by three-shock theory. The transition criterion (several of them, actually, based on the assumption of ideal gases and self-similar flow) is discussed in Ben-Dor (1992).

There are six data points in Figure 3.1 and one data point in Figure 3.2 that do not have associated error bars. Heilig and Reichenbach present these data but the absence of error bars is not explained. We assume that absolute error bars similar to those that are given for the other data points should be attached to these points, but we do not directly illustrate such an inferred error bar.

The presented error bars should not be interpreted as quantifying overall experimental uncertainty, which is really not discussed by Heilig and Reichenbach. Even restricted to

diagnostic resolution quantification Heilig and Reichenbach do not present a probabilistic interpretation of their error bars. It is unlikely that a uniform distribution is an adequate interpretation of these error bars, for example, given the asymmetry of the upper and lower bound of their representation about the nominal experimental value.

It is known that the reflection transition regime is especially sensitive to factors that properly enter into experimental variability (Ben-Dor and Glass, 1979; Heillig and Reichenbach, 1984; Ben-Dor, 1992). These factors include real gas effects, especially viscosity, near the vertex of the wedge; sensitivity to the finite extent of the wedge vertex; sensitivity to surface roughness of the wedge; and sensitivity to the temperature of the wedge. The finite thickness of the pressure gauges is not discussed at all in Heillig and Reichenbach's paper, but it may also contribute to some experimental variability. The lack of discussion of overall experimental variability is typical in our experience in relation to existing published experimental data for purposes of validation. Only dedicated validation experiments can really hope to improve information about experimental uncertainty.

Heilig and Reichenbach note that viscous effects in the gas flow near the finite wedge apex, basically a boundary layer effect, may increase the transition angle of incidence for RR to MR by two to three degrees when compared to predictions of two- and three-shock theory. If true, this implies that the prediction of the transition angle of incidence in our ALEGRA calculations will be too small by two to three degrees as compared to the data. Ben-Dor and Glass (1979) also observe that non-self-similar real gas effects make the transition from RR to DMR more complex.

Ben-Dor and Glass (1979), Figure 21 summarize the experimental transition region for air, oxygen, and nitrogen in their paper. For shocks in air with Mach numbers 1.37 and 3.36, the transition angles of incidence are given by approximately 43 degrees (RR → MR) and 41 degrees (RR → DMR) respectively. The latter angle does not fully agree with the data from Heilig and Reichenbach plotted in Figure 3.2. This suggests the difficulty in experimentally measuring the transition angles precisely.

3.2 Comments on Validation Metrics

Trucano, *et al*. (2001) has presented a general framework for validation metrics, with a complementary discussion found in Easterling (2001). Broadly speaking, by validation metrics we mean the techniques by which we compare calculations and experimental data; and the methodology used for assessing the meaning of such comparisons.

For shock wave problems of the type discussed in this paper we have four general methods of comparison between calculations and experimental data.

- We may perform qualitative comparisons of 2-D flow fields. Primarily this means to qualitatively compare the presence of flow field structures such as the reflected

shock, Mach stem, second Mach stem, and so on from experimental data such as Schlieren images and shadowgraphy.

- We may study qualitative agreement, such as trends and orders of magnitude, with more quantitative data, in this case experimental pressure ratio data.

- We may study the quantitative agreement of the calculations with the quantitative experimental data, specifically assessing agreement of calculations within specified experimental data error bars.

- We may study the quantitative agreement of the 2-D flow fields of the calculations with those of the experiments. For example, we could compare with experimentally measured 2-D density contours.

In this report we examine qualitative agreement with published flow fields, but do not present the details of this directly. The reason is that while some flow field images are available (Heilig and Reichenbach, 1984; Ben-Dor and Glass, 1979) and have been presented in Sandoval (1987) we do not have decent quality reproductions of the schlieren images available for presentation in this report. Thus, we will only comment on the most obvious features of qualitative comparison available.

Our primary focus for experimental comparison, as was Sandoval's, is the quantitative comparison of our computed pressure ratios with the reported pressure data of Heilig and Reichenbach summarized in Figures 3.1 and 3.2. Thus, we seek to make closer comparison with these data than simply to confirm agreement with trends in the data. Complete success in such a comparison is defined by our best estimate calculations lying within the reported experimental error bars. Partial success, which is in fact sufficient for the goals of the present study, is defined by having good qualitative agreement with the data, including overall trends, partial quantitative agreement, and a well-founded belief that the calculations will improve in accuracy over some range of experimental data either through bias correction or improved computational resolution or both.

Quantitative comparison with 2-D flow fields will not be addressed in our current work. There are published isopycnic data for regular, Mach, and double Mach reflections in Ben-Dor and Glass (1979). (Such data are not reported in Heilig and Reichenbach.) Because we must consider data that have been previously published rather than acquired through an ongoing dedicated validation activity, we would have difficulty quantifying the images published by Ben-Dor and Glass to the degree necessary for a completely quantitative comparison. Also, because the modeling strategy used in this report that takes advantage of self-similarity of ideal gas shock reflection problems would have to be modified to allow quantitative comparison with accurate experimental density contours. Finally, real gas effects influence the work that Ben-Dor and Glass report. To fully compare with their published data we would need to perform calculations with real gas equations of state (such as tabular equations of state), which introduces an additional element of complexity in the validation process.

The data studied in this work also offer the opportunity to apply techniques such as those used in Hills and Trucano (2001). Multivariate extensions of the work of Hills and Trucano are presently under study and must be pushed further before we can hope to apply them to a study like our present one. In addition, refined statistical comparisons will also demand more attention to calculation verification and uncertainty than we have mustered in this report.

All of these possible validation metrics would receive different emphasis for other kinds of validation problems involving shock reflections, such as might occur in radiation-magentohydrodynamics validation. For example, quantitative comparison with 2-D and 3-D flow field data may be a critical element of success in such validation, and could not be avoided as we will here. One advantage of dedicated validation experiments, which will likely be the case in more complex validation activities, is the ability to significantly strengthen assessment criteria in the validation exercise because more quantified validation data are more readily available.

3.3 Agreement With Trends and Partial Quantitative Comparisons

Once again, we will state that in the ideal gas treatment of shock reflection, the details of the shock reflection process depend only on the ideal gas gamma, the shock incidence angle, and the Mach number of the incident shock. We want to assess the ability of ALEGRA to model the transitions from one domain of reflection to another, as well as accurately model reflection for each fixed wedge angle of interest.

For a fixed Mach number and ideal gas gamma, a reflection transition occurs as we vary the angle of incidence. For a fixed Mach number of 1.37, we have compared experiment and calculation in Figure 3.3. This figure is the same as Figure 3.1, except that we have added discrete computational pressure ratios from ALEGRA. These calculated pressure ratios are also summarized in Table 3.1. We first note that for the Mach 1.37 suite of calculations a transition from regular reflection, which occurs at lower incidence (higher wedge) angles, to Mach refection at higher incidence (lower wedge) angles, occurs around an incidence angle of 43 or 44 degrees. Our computed transition angle is thus approximately equal to the transition angle suggested by Heilig and Reichenbach's data in Figure 3.1, as well as the data in Ben-Dor and Glass, by about three degrees. Overall, our calculation results are in qualitatively good agreement with the experimental data in that the slope trends observed in the experimental data are mainly mirrored by our calculations, except in the region of the experimental flow transition, where the slope of our computed results is apparently too flat. Our earlier figures in Section 2 demonstrated that the qualitatively correct differences (as described in Figures 2.1 – 2.3) of the 2-D flow fields for regular and Mach reflection are captured in our calculations.

We also scrutinize our quantitative comparison with the experimental data in Figure 3.3. The quantitative data compare experimental and calculated values of the pressure ratios defined in equations (2.5) and (2.6). We are able to simulate the pressure ratios at incidence angles well away from the flow transition quite well. Our quantitative pressure

ratios seem to lie within the data error bars (which have to be guessed for the incidence angles greater than 45 degrees) for these angles. Our quantitative disagreement with the data in the flow transition region may well be due to our difficulty in analyzing the calculated results to extract the pressure ratios (see our comments below). IDL (Research Systems, 1998) was used to calculate this information from the corresponding ALEGRA simulations. A sample IDL input deck that we used to produce Figure 3.3 is given in Appendix A. Due to computational problems that we will discuss further, care must be applied in the selection of values of p_1 and p_2 for use in equations (2.5) and (2.7).

For the Mach 3.36 calculation, the calculated transition from regular reflection to double Mach reflection occurs around an incidence angle of 42 degrees (Figure 3.4). Once again, the qualitative comparison of the calculations with the experimental data is quite good. In our 40-degree incidence angle calculation, we observe a regular shock reflection. In Sandoval's calculations (Sandoval, 1987) a double Mach stem is computed down to incidence angles of around 35 degrees. We appear to agree better with the given experimental data than the Los Alamos calculations. Sandoval notes that this is a tricky experimental region for accurately determining the flow transition angle.

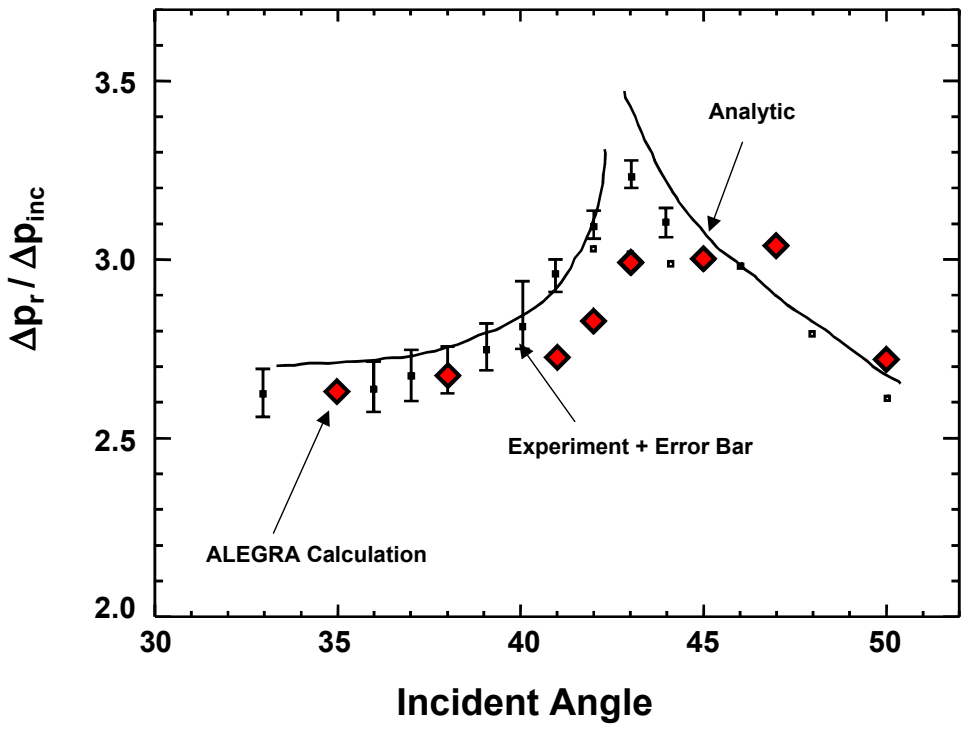

Figure 3.3 Plot of ALEGRA calculation results, experimental data and analytic solution for Mach 1.37 calculation at various incidence angles.

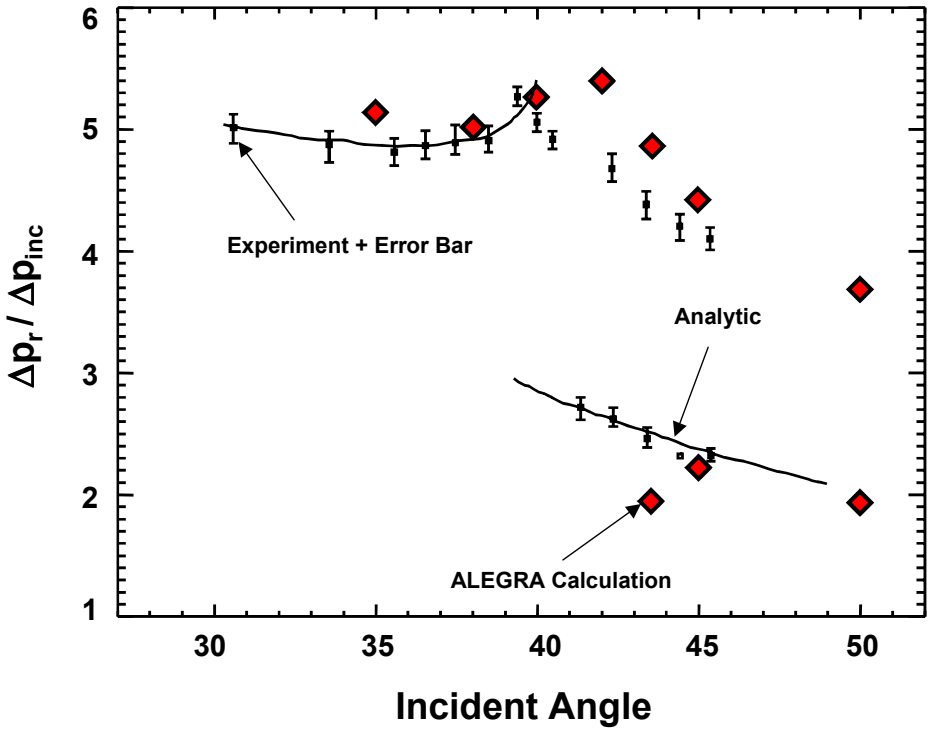

Figure 3.4 Plot of ALEGRA calculation results, experimental data and analytic solution for Mach 3.36 calculation at various incidence angles.

The quantitative data comparison between the experimental and calculated pressure ratios (using equations (2.5), (2.7), and (2.8)) in Figure 3.4 is fairly good. One anomaly appears to be the pressure ratio for the first Mach stem at the 43.5-degree incidence angle. Due to computational problems that we will discuss further, care must be applied in the selection of values of p_1, p_2 and p_3 for use in equations (2.5), (2.7), and (2.8). The anomaly at 43.5 degree could well be an artifact of the choices we make for p_2 in reducing the computational data. Because the error bars for the experimental data in Figure 3.4 are smaller than in Figure 3.3, a smaller percentage of our computed data lie within the experimental error bars. However, we are in better quantitative agreement with the experimental data near the low transition.

Table 3.1 Summary of nominal computational pressure ratios.

Mach Number	Incidence Angle	$R^{(1)}$	$R^{(2)}$	$R^{(3)}$
1.37	50		2.72358	
1.37	47		3.03201	
1.37	45		3.03711	
1.37	43		2.98049	
1.37	42		2.83797	
1.37	41	2.73113		
1.37	38	2.67764		
1.37	35	2.63737		
3.36	50		3.67682	1.92439
3.36	45		4.41242	2.21543
3.36	43.5		4.88101	1.94758
3.36	42		5.40264	
3.36	40		5.25642	
3.36	38		5.03454	
3.36	35		5.12156	

3.4 Computational Pressure Ratio Variability

Calculating the pressure ratios from the computed pressure plots along the surface of the reflecting wedge for comparison with the experimental data is not a trivial task. The data reported in Figure 3.3 and 3.4 represent our choice of specific points from a range of plot points.

Figures 2.9 (b), 2.12 (b), and 2.16 (b) show the complexity of the computed pressure plots for RR, MR, and DMR. These figures all show that significant variability in the computed pressures behind the various shock waves in the problems has to be accounted for in calculating pressure ratios. We replicate these figures below to illustrate the methods we used for deciding upon ***nominal*** computed values of the pressure ratios for the three flow reflection regimes.

Consider the zoom of the pressure plots for the regular reflection calculation 1.37_55 in Figure 3.5. Two points are there emphasized for possibly computing the pressure ratio from this plot – the maximum pressure and the pressure seven zones behind the maximum. We believe the peak pressure value contains an overshoot, as well as a mild post-shock oscillation, which are artifacts of the artificial viscosity in ALEGRA. The value seven zones behind the apparent peak pressure lies in an almost constant post-shock

state. If the calculation were ideal, the pressure amplitude of the shock wave would equal the pressure value in the far field. We believe that the pressure value seven zones behind the leading edge of the shock wave is a more numerically accurate value of the pressure to use to define p_1 in calculating the pressure ratio $R^{(1)}$ than the peak pressure. This is the way we calculate $R^{(1)}$ for RR and all the values shown in Figure 3.3 and 3.4.

This choice strongly influences how well our particular calculations agree with the experimental data. We illustrate this potential variability in our calculated pressure ratios in Figure 3.6 (a), where we have plotted the value of $R^{(1)}$ resulting from the choice of the peak pressure, the seven zone off-set, the experimental value, and the experimental error bar for the flow defined in Figure 3.5. The post-shock pressure ratio value is almost identical to the experimental value, while the pressure ratio defined by choosing the peak pressure value falls well outside the experimental error bar.

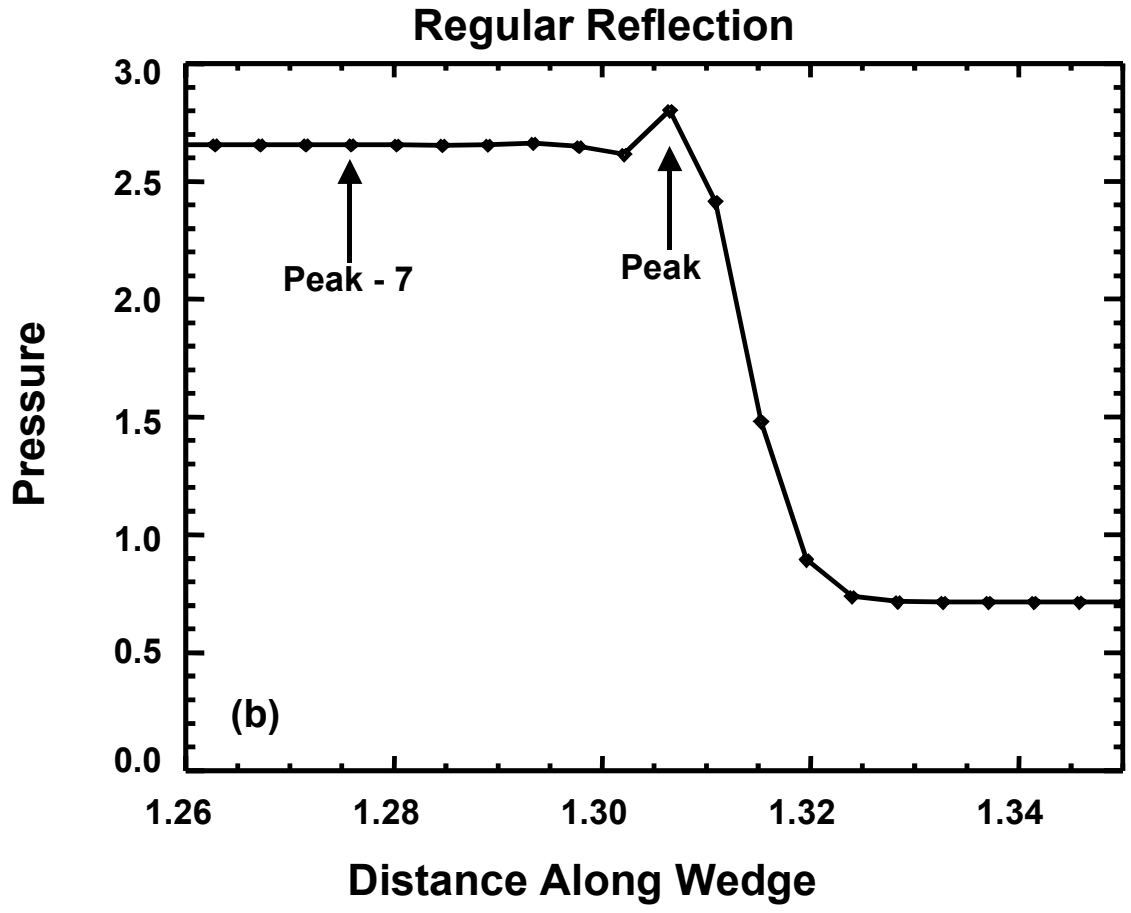

Figure 3.5 Zoom of the pressure plot along the wedge for the regular reflection problem with Mach number of 1.37 and incident angle of 35 degrees.

Figure 3.6 (b) plots this information as a type of relative error that includes a compensation for the experimental error bar. The percent relative error in Figure 3.6 (b) is calculated using the following formula:

$$E = \frac{D}{e} \times 100, \quad \text{if } D > 0$$
$$= 0, \quad \text{if } D = 0 \tag{3.1}$$

where D is the distance of the computed pressure ratio from the experimental error bar, and e is the length of the experimental error bar on the side of the numerical value. This would equal half the total length of the error bar if the error were symmetrical about the nominal experimental value. Equation (3.1) is only one possible choice for quantifying differences between calculation and experimental data. The general topic of such differences as validation metrics is stressed in Trucano, *et al*. (2001). There is clearly no probabilistic interpretation of the equation (3.1) in the present case because we do not have sufficient information about the probabilistic interpretation of the experimental error bars.

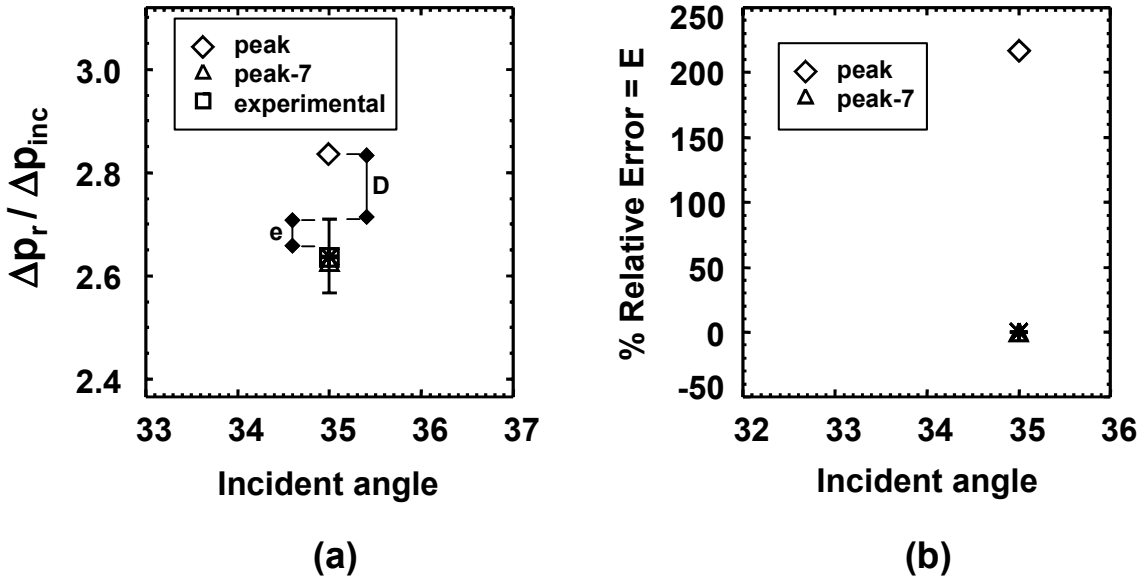

Figure 3.6 Plot of (a) ALEGRA calculated $R^{(1)}$ and experimental data with the error bars and (b) the corresponding percent relative error for the regular reflection, Mach 1.37 calculation with an incident angle of 35 degrees. We have shown graphically how e and D are defined in (a).

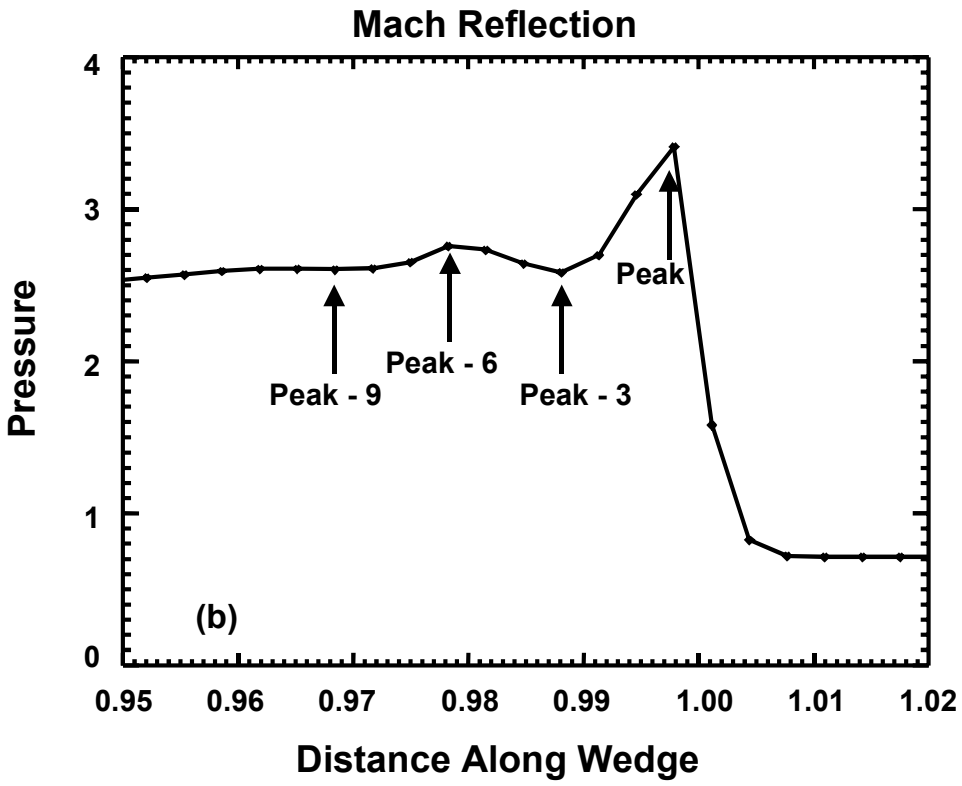

Figure 3.7 Zoom of the pressure plot for the Mach shock reflection calculation with a Mach number of 1.37 and incident angle of 50 degrees.

We face similar difficulties for the other shock reflection regimes. For the Mach reflection problem, choosing which points to sample was not as straightforward as the regular reflection case. The pressure plots along the wedge for the Mach 1.37, 50-degree incident angle are plotted in Figure 3.7. The maximum pressure, as well as the pressure at locations three, six, and nine zones behind the peak pressure zone, was used to compute the pressure ration $R^{(2)}$. These three points correspond to the semi-constant plateau region behind the peak pressure in the Mach stem. The process of extracting the data and calculating the pressure ratio values is the same as described above for the regular reflection. Figure 3.8 shows the variability of calculated pressure ratios, the experimental nominal value and its associated error bar, and relative percent errors calculated using equation (3.1). Only the pressure ratio derived from the maximum peak pressure strongly deviates from the experimental data. The nominal pressure used for reporting calculated pressure ratios in the Mach reflection regime is the value of the data point nine zones behind the peak pressure, where the data are most constant. But this flow region is not characteristic of a simple constant planar shock, and so there is a real question about whether this is the most appropriate value to deem to be nominal. The problem would be removed if there were no numerical overshoot to worry about at the Mach stem proper.

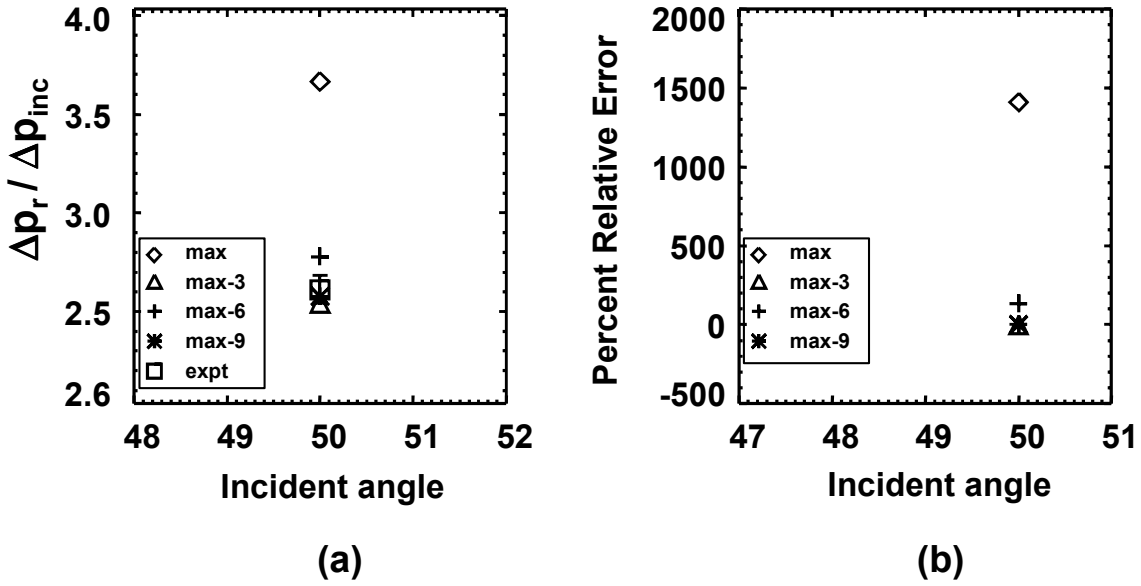

Figure 3.8 Plot of (a) experimental data with the error bars and ALEGRA and (b) the percent error for the Mach reflection, Mach 1.37 calculation with an incident angle of 50 degrees.

We emphasize one feature of Figure 3.8. The experimental data for the 50-degree incident angle given in Figure 3.1 does not have an error bar. Thus, for notional purposes we simply assumed an error bar for this particular data that was the same as the last visible error bar near incident angle of 44 degrees. There is no basis for this choice; it is simply convenient for applying our relative error measure in this case.

In the double Mach reflection problem, choosing which points to sample was not as straightforward as for the regular reflection or single Mach reflection cases. The pressure plot along the wedge for the Mach 3.36, 45-degree incident angle is plotted in Fig 3.9. This plot shows a complex structure behind the first Mach stem. Oscillations, which are undoubtedly artifacts of the artificial viscosity, contribute to this structure, but are harder to localize for purposes of selecting nominal pressures for computing pressure ratios. The maximum pressure was chosen, along with the location eleven zones behind the peak pressure, for computing the pressure ratio $R^{(3)}$. The pressures thirteen, fifteen, and twenty-two zones ahead of the peak pressure were used to compute the pressure ratio $R^{(2)}$. These results are summarized in Figure 3.10 (a). Once again, as noted in the other reflection cases above, only the maximum peak pressures corresponding to the two Mach stem fronts deviate greatly from the experimental data. The data value taken eleven zones behind the maximum pressure of the second Mach stem is much closer to the experimental data than the maximum pressure.

The difficulty in selecting an appropriate nominal value is that there is no clear constant pressure plateau in the post-shock region of either Mach stem. The general trend around the second Mach stem is for decreasing pressures. If another location were chosen further away it would produce a pressure ratio even closer to the experimental data. The selection problem is even more difficult behind the first Mach stem because of the general irregularity in the pressure data. One possibility for defining a nominal value that we did not explore would be to average pressure values over a set of zones close to yet behind the first Mach stem. This approach could also be applied to extracting the nominal value behind the second Mach stem. The main thing we wish to emphasize in this discussion is that there is difficulty associated with fully analyzing the calculated values that is associated with lack of verification, in particular solution convergence, of the particular calculations under scrutiny.

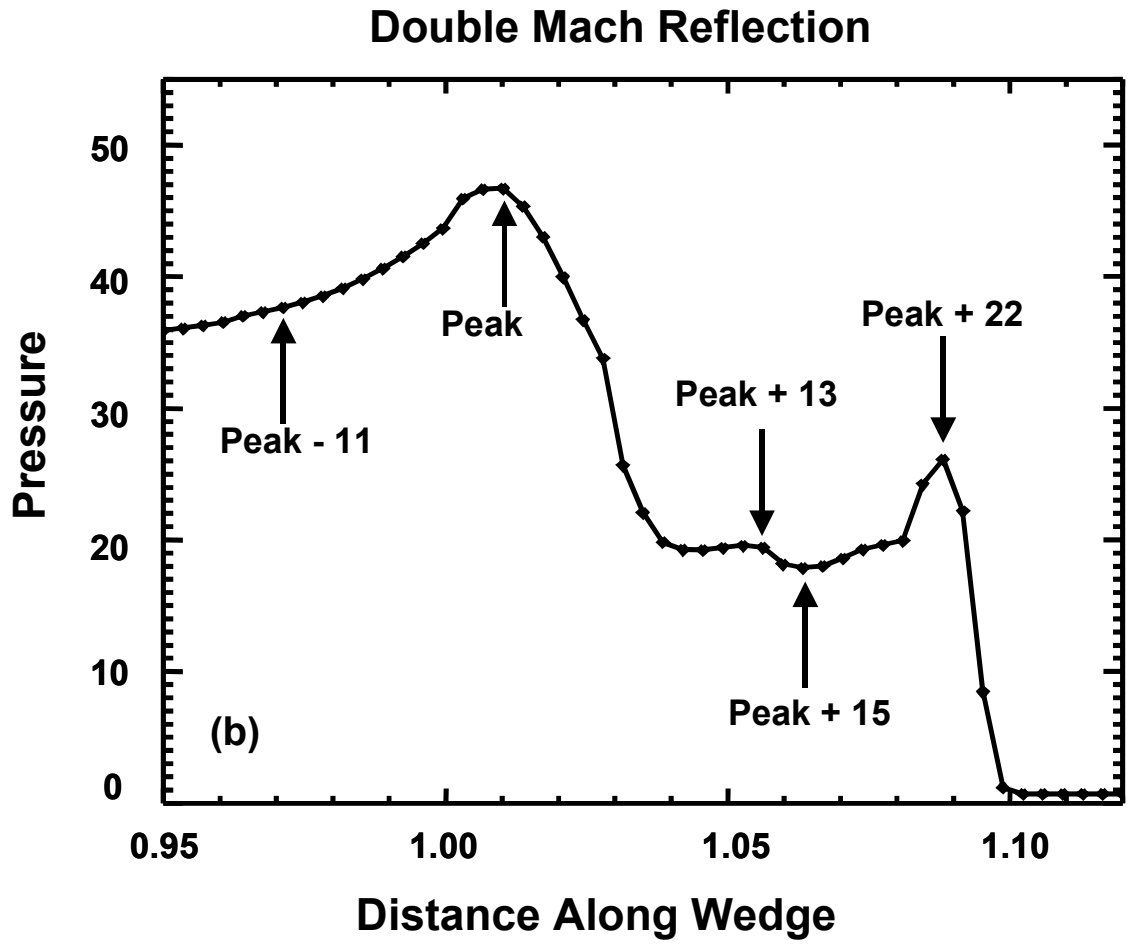

Figure 3.9 Zoom of the pressure plot for the double Mach shock reflection calculation with a Mach number of 3.36 and incident angle of 45 degrees.

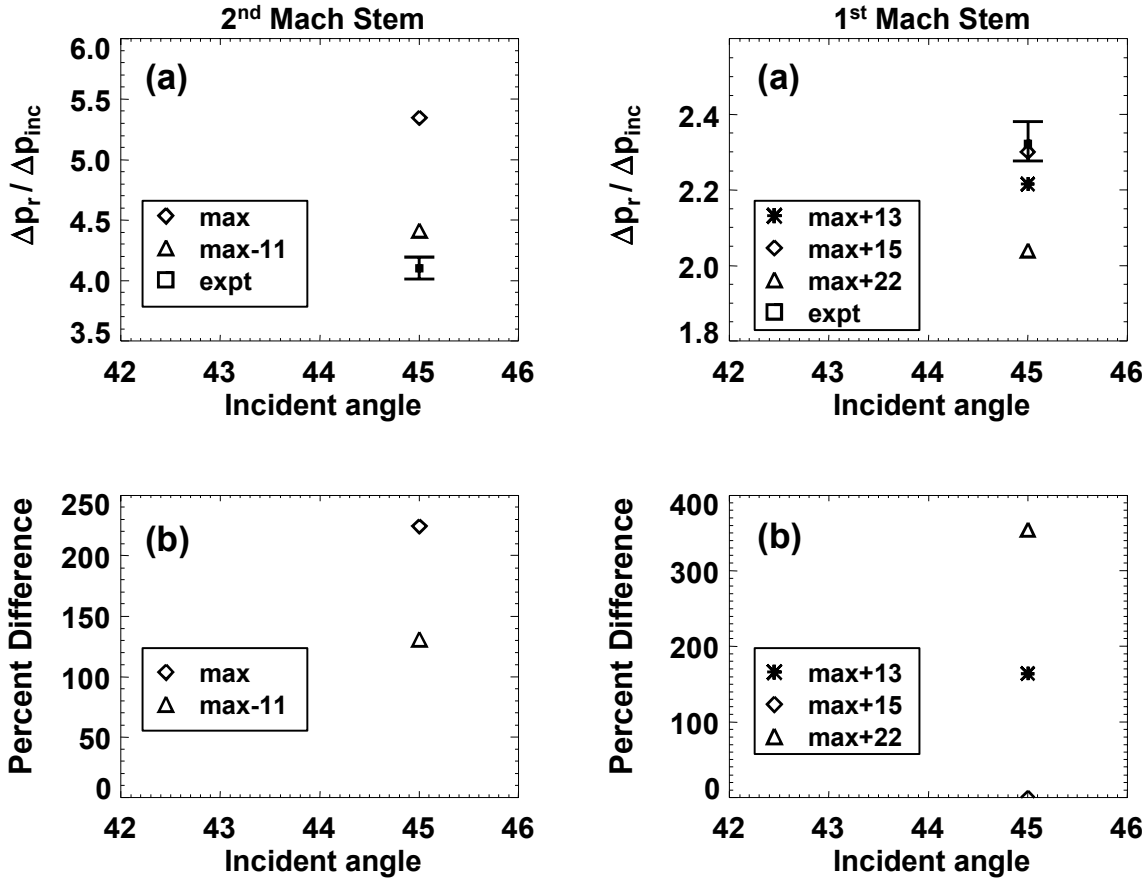

Figure 3.10 Plot of (a) experimental data with the error bars and ALEGRA calculations and (b) the percent error for the double Mach reflection, Mach 3.36 calculation with a wedge angle of 45 degrees.

In conclusion, we stress that the nominal computed values of the pressure ratios $R^{(1)}$, $R^{(2)}$, and $R^{(3)}$ shown in Figures 3.3 and 3.4 are rational. They also show the best agreement with the experimental data when variability uncertainty in the plot data is analyzed as above. Experimental data trends, including the reflection regime transitions, are accurately simulated. In some, but not all cases, the nominal computed values in RR, MR, and DMR lie within the experimental error bars.

However, there are clearly questions remaining about the quality of the computed data. In particular, the adequacy of this variability analysis, and its coupling to uncertainty associated with calculation verification, must be questioned. We now examine the robustness of our computed pressure data to other verification issues, including grid

resolution. This sheds additional light on the quality of the nominal calculated values of the pressure ratio in Figures 3.3 and 3.4.

3.5 Calculation Verification and Computational Uncertainty

3.5.1 Convergence

One important component of calculation verification for validation studies is convergence assessment. We know that the resolution of the grid affects our calculations dramatically. Without high resolution as presented in Table 2.1 we do not even see the formation of MR and DMR regimes in our calculations. Sensitivity of our pressure data to resolution is shown in Figure 3.11, which overlays the pressure plots from the low, mid, and high resolution Mach 1.37, 35-degree incidence angle calculations. For the regular reflection, the lowest zoning is all that is needed to observe the important shock structure. But from Figure 3.11 we can see that at lower resolutions the shock front is quite spread out. The pressure peak also seems to be higher for the lower resolution calculations, clear evidence of the influence of the shock front overshoots and post-shock oscillations associated with the artificial viscosity. This suggests that convergence in pressure just behind the shock front, the ideal location for extracting the pressure for the pressure ratio calculation, is problematic as long as the post-shock oscillations are not tamed. The post-shock plateau in the pressure can be observed for each calculation resolution, but it is flattest in the highest resolution calculation. The post-shock pressure in the finest zoned calculation is clearly not equal to the pressure observed at the shock front itself due to oscillations.

Grid resolution affects the single Mach reflection calculation dramatically. Figure 3.12 plots overlays of the pressure plots from low, mid, and high-resolution calculations of the Mach 1.37 calculation with an incidence angle of 50 degrees. For Mach reflection, the coarsest zoning is all that is needed to observe the Mach stem as a single discrete structure. But as can be seen from Figure 3.12, the shock front is more spread out and the peak pressure peak is reduced for the two lower resolution calculations. The lower resolution calculations do not have the oscillations that are observed behind the Mach stem in the highest resolution calculation. Strangely enough, the coarse and high-resolution calculations have equal pressures far behind the shock front. The medium resolution calculation's pressure far behind the shock front is lower. This demonstrates that the convergence studied using coarse, medium, and fine resolution for MR is not in the asymptotic (monotone) regime (Roache, 1998). We need to refine our finest calculations to make further statements about convergence.

Our difficulty increases in the double Mach reflection regime. Figure 3.13 is a plot which overlays the pressure plots from low, mid, and high-resolution calculations for the Mach 3.36 calculation with an incidence angle of 45 degrees. For double Mach reflection, only the highest grid resolution was sufficient to observe the double Mach stem structure. The shock front is once again too diffused for the two lower resolution calculations. The lower resolution calculations do not have the oscillations that are observed behind the

shock in the highest resolution calculation. Once again, convergence of the post-Mach region is not monotonic for our three different resolutions. We basically have not even begun a convergence study on this problem because the double Mach region has only just appeared at our finest resolution.

There are important reasons to converge calculations so that the asymptotic region has been accessed computationally. Empirical order of convergence and extrapolated error prediction (such as performed using Richardson extrapolation) in the limit of zero grid spacing can be assessed in the asymptotic region. See (Roy, *et al*., 2000; Roy, 2001) for an illustration of these concepts for gas dynamic flows. Using grid resolutions that doubled (or greater) our finest grid resolution reported in Table 2.1 is clearly required. It was beyond the scope of our current work, but clearly calculation verification remains an open question.

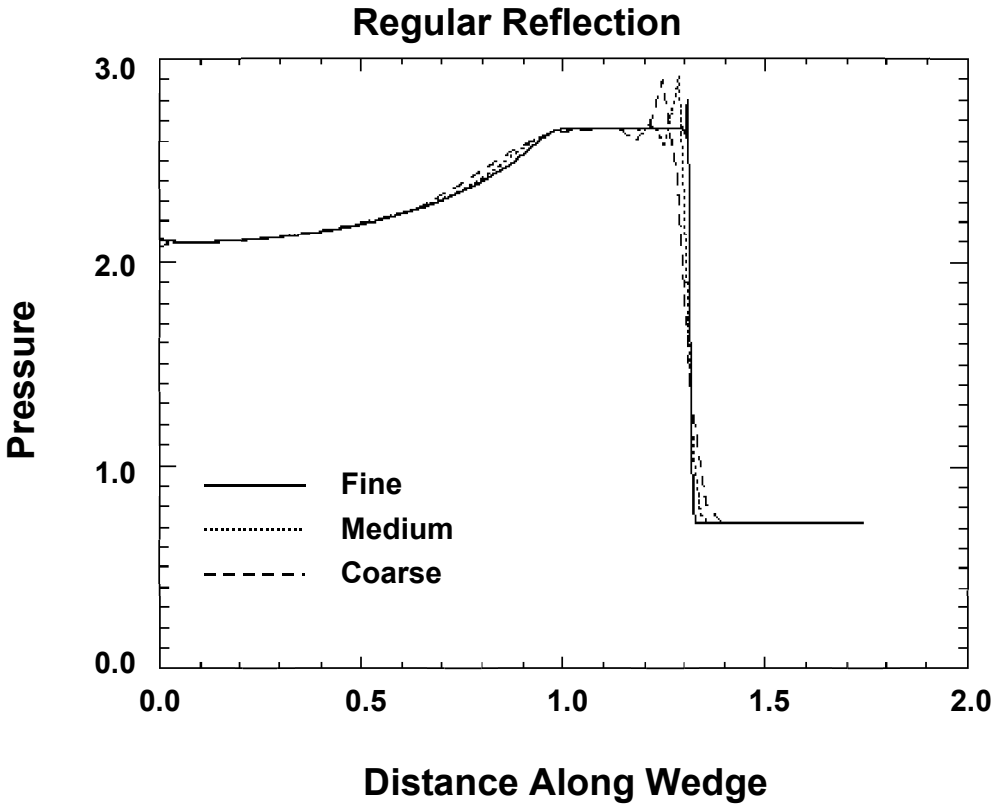

Figure 3.11 Plot of pressure plots of the regular reflection calculation with Mach number 1.37 and wedge angle 35 degrees for coarse, medium, and fine grids.

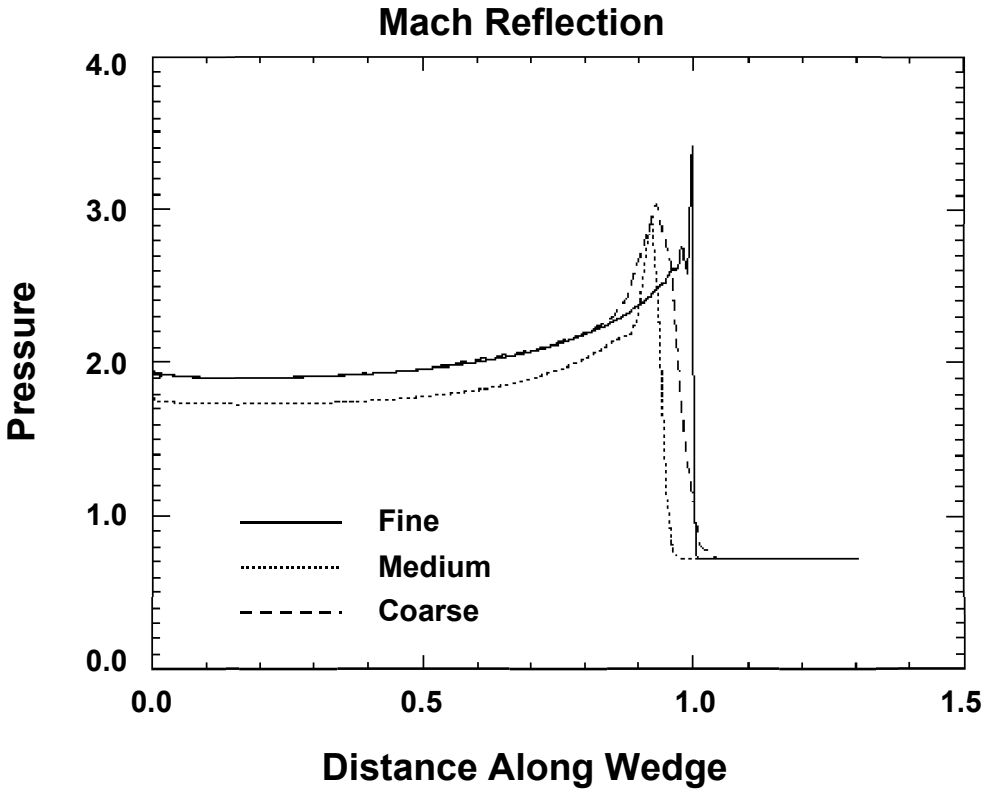

Figure 3.12 Plot of pressure versus distance of the regular reflection calculation with Mach number 1.37 and wedge angle 50 degrees for coarse, medium, and fine grids.

3.5.2 Comparison Difficulties

One of the difficulties with validation is the complexity of comparing computational results directly with experimental data and insuring proper alignment of the calculations to insure that this comparison is optimal. For example, in the current experiments, exact integer angles for the wedges were not used in the experiments, while we used integer angles in our calculations. This is because the initial motivation for our work was to assess the capability of ALEGRA to correctly model the qualitative shock wave reflection transitions RR → MR and RR → DMR. This then accounts for additional error in our difference comparisons with the experimental data since we are actually interpolating our comparison with the experimental data in Figures 3.3 and 3.4. To illustrate and quantify the maximum differences that we may be looking at due to dissimilar angles, we re-ran our calculation that had the largest difference in alignment with the experimental angles. The calculation we chose was the Mach 1.37, 35-degree incidence angle RR problem. The exact experimental incident angle (Heilig and Reichenbach, 1984) was 35.98 degrees, which accounts for a difference of 0.98 degrees between the experiment and our nominal calculation. This does not seem to be a large difference on the face of it, especially since we are well away from the flow transition threshold angle. However, it is

worth confirming that this is the case, if for no other reason than to demonstrate robustness in our calculated results.

We ran the 35.98-degree calculation with the highest grid resolution in Table 2.1. The calculation pressure plots for the 35.98 and 35 degreee calculations are plotted against each other in Figure 3.14 (a). The major difference in these two plots is a small difference in the timing of the shock. The shock from the 35.98-degree incidence angle calculation had a slightly smaller velocity component along the wedge than the 35-degree calculation, which is fully consistent with the geometry of shock incidence. We compare the nominal computed pressure ratios of the two calculations with the nominal experimental data and error bar in Figure 3.14 (b). Interestingly, the nominal value for the calculation that exactly replicated the experimental wedge angle has a slightly greater error. However, this computational value still lies within the experimental error bar, as is the original calculation. One interpretation of this result is that the experimental error bar is insufficient to contrast pressure ratio data for small differences in wedge geometries.

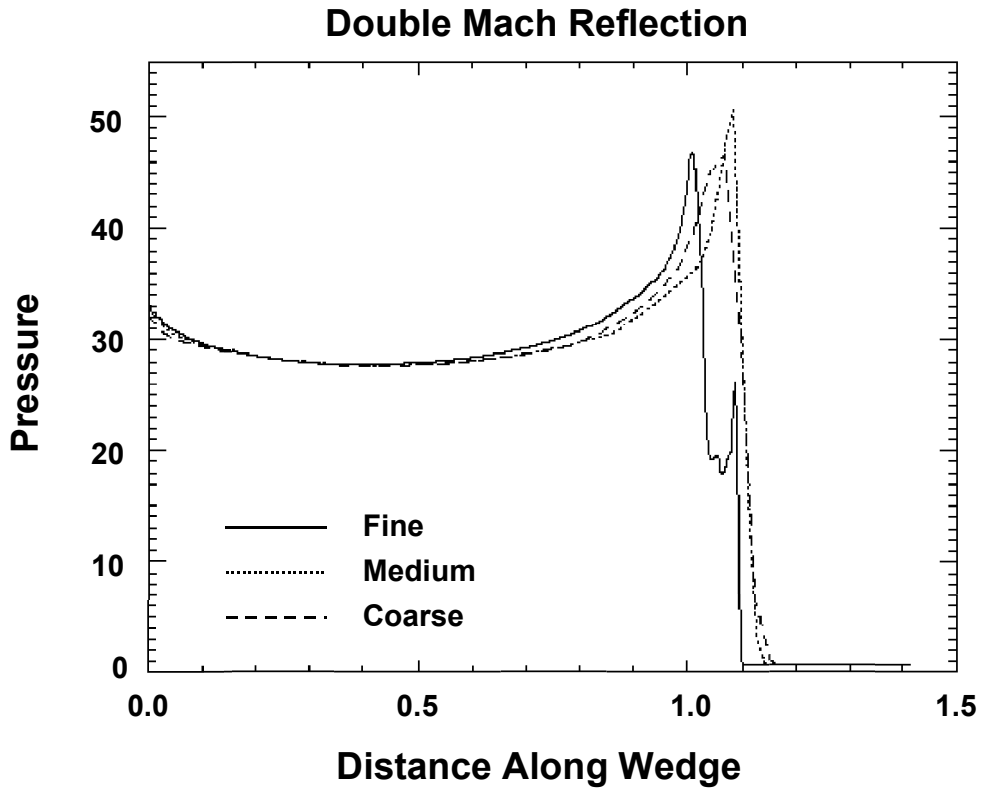

Figure 3.13 Plot of pressure versus distance of the regular reflection calculation with Mach number 3.36 and wedge angle 45 degrees for coarse, medium, and fine grids.

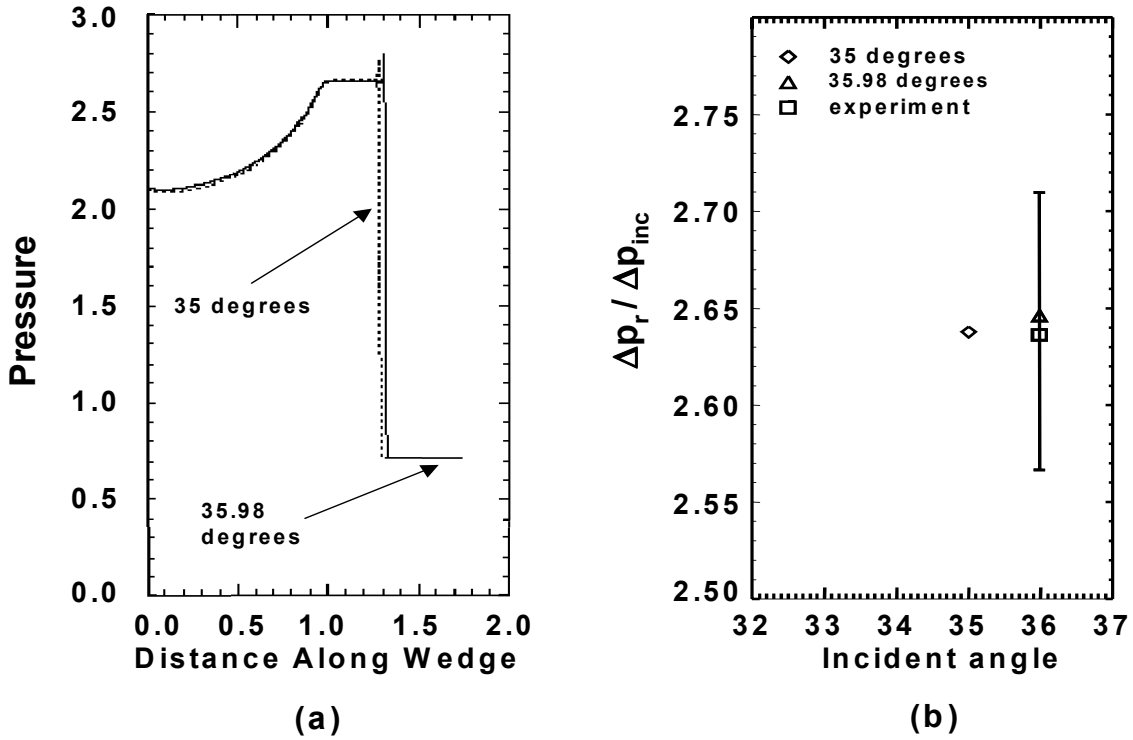

Figure 3.14 (a) Pressure versus position plots along the wedge for mach 1.37 calculation with incidence angles of 35 degrees and 35.98 degrees. (b) The comparison of experimental data with the same calculations.

3.5.3 Plot Sensitivity

Given the complexity of choosing computed pressure values for calculating pressure ratios, another area of concern in our computational-experimental comparisons is whether or not the exact position taken for the plots can drastically change the calculated results. This is primarily a robustness concern.

We address this question by examining different pressure plot offsets from the surface of the wedge. We select the Mach 1.37, 35-degree incident angle fine resolution RR calculation and plot pressure on the wedge surface, and two and four zones offset in the direction perpendicular to the wedge surface in Figure 3.15. These plots are almost indistinguishable, with a slight amount of variability obvious at the shock front.

Similar plots for MR and DMR are presented in Figures 3.16 and 3.17. In Figure 3.16, the agreement is once again quantitatively good between the surface pressure plot and the 2 and 4 zone offset pressure plots for the Mach reflection calculation (Mach 1.37, 50 degree incidence angle). Once again, these plots are almost indistinguishable, with small variability apparent at the shock front.

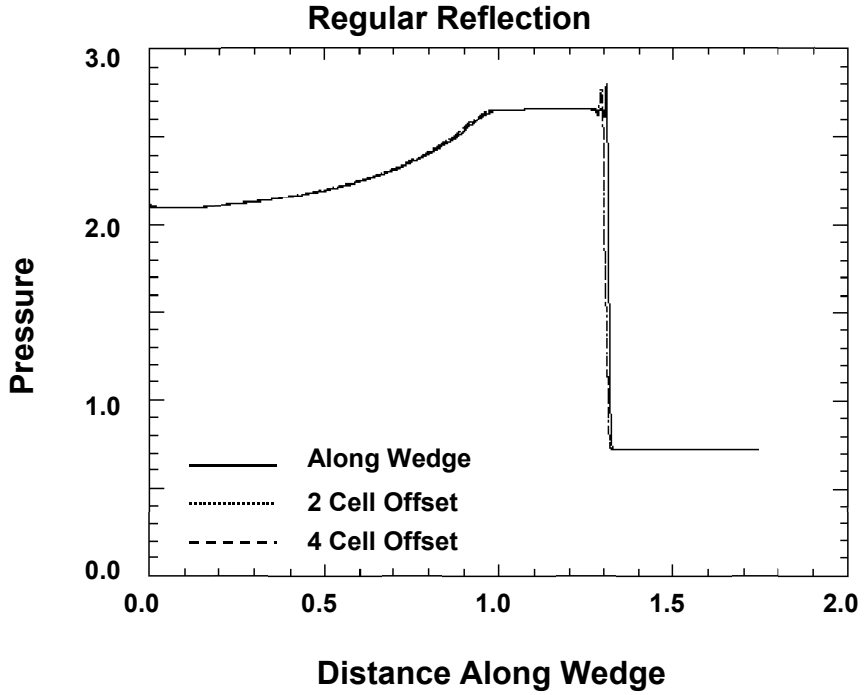

Figure 3.15 Pressure versus position plots along the wedge for the Mach 1.37 RR calculation with incident angle 35 degrees at various positions: surface of wedge, 2 zone offset, and 4 zone offset.

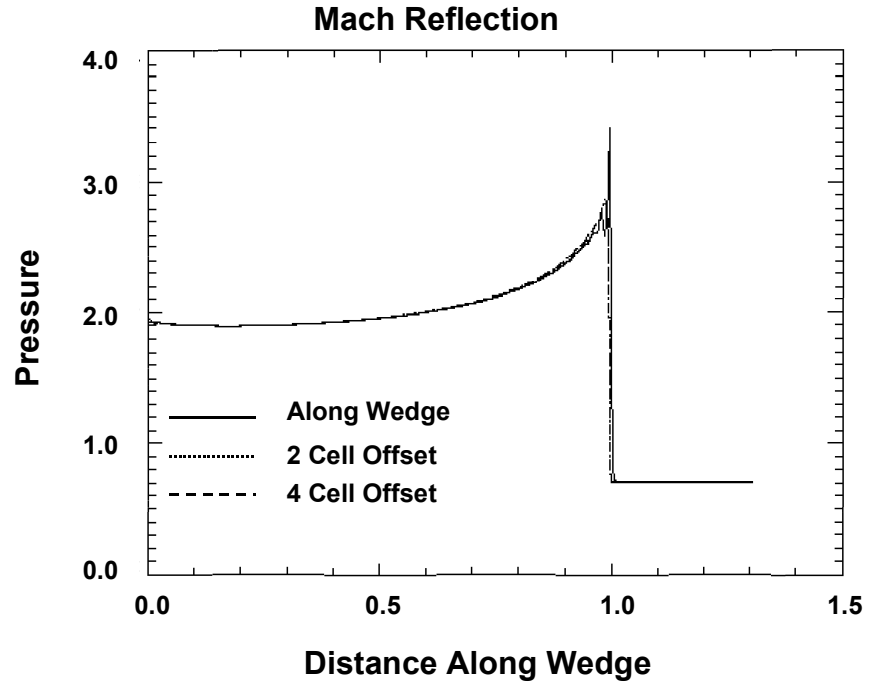

Figure 3.16 Pressure versus position plots along the wedge for the Mach 1.37 MR calculation with incidence angle 50 degrees at various positions: surface of wedge, 2 zone offset, and 4 zone offset.

The plot agreement in Figure 3.17 for the double Mach reflection calculation (Mach 3.36, 45 degree incidence angle) is not as good. There is a significant difference in timing between the surface pressure plot and the offset pressure plots, as well as a difference in peak pressure at the second Mach stem that appears to be more than simply an overshoot phenomenon. This suggests that there may not be adequate resolution (still) in the direction normal to the wedge in the current fine meshed DMR calculation.

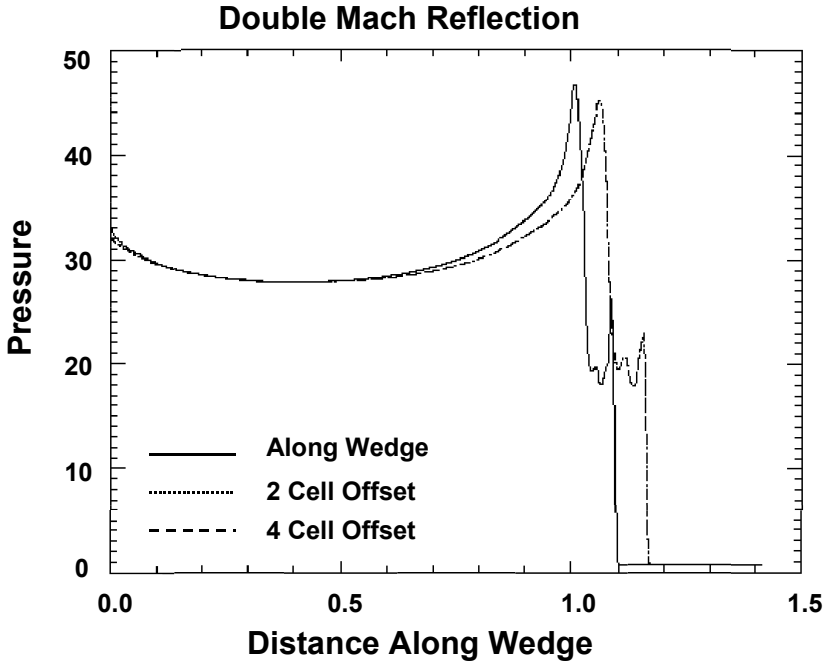

Figure 3.17 Pressure versus position plots along the wedge for the Mach 3.36 DMR calculation with incidence angle 45 degrees at various positions: surface of wedge, 2 zone offset, and 4 zone offset.

4. Discussion

In this report we have summarized the results of a validation assessment of strong shock wave Eulerian hydrodynamics for the ALEGRA shock wave physics code. This assessment focused on oblique shock wave reflection phenomena in three distinct regimes and the associated flow transitions: regular reflection, Mach reflection, and double Mach reflection. The main purpose of this work was to develop evidence of ALEGRA capability and credibility for accurate calculation of physical shock wave phenomena of relevance to high energy density physics applications, especially for Z-pinch studies. As such, the current work is only one of many potential validation assessment activities that are required to fully evaluate the credibility of ALEGRA radiation-magnetohydrodynamics simulations.

We presented results demonstrating that ALEGRA is in good qualitative agreement with pressure ratio data gathered for oblique shock wave reflection, including agreement with data trends (signs of data curve slopes) as a function of shock incident angle, as well as the reflection regime transition angles from RR to MR and RR to DMR. The original goal of our study was to simply illustrate the capability of ALEGRA to calculate shock reflection phenomena in all three regimes, with the secondary goal of assessing the code's ability to describe the transition angles. As we pursued the work it became clear that we could rationally study the quantitative agreement of the ALEGRA with the selected experimental data. We found that in some situations highly resolved ALEGRA calculations produce nominal data that fell within the error bounds of the corresponding experimental data. In other situations this was not the case.

There are significant uncertainties associated with our nominal calculation data that we compared with experiment that seem to primarily reside in code and calculation verification issues. First, we argued that shock front diffusion, overshoots, and post-shock oscillations associated with the current artificial viscosity implementation in ALEGRA made the quantitative determination of our nominal computed pressure ratios difficult. We discussed the choices we made in determining these nominal values from the raw pressure data taken from the code in the form of pressure plots along the surface of the computational reflection wedge. While our nominal definitions are consistent with acceptable post-shock behavior and happen to also be in good agreement with some of the experimental data we analyzed, a goal for future work should be to eliminate some of the artifacts associated with the artificial viscosity so that the current wide scope for interpretation of post-shock data is significantly narrowed. It is unlikely that further grid convergence ***alone*** will be sufficient to accomplish this goal.

Second, we observed that our grid convergence was itself probably inadequate. We saw evidence for non-monotonic convergence for the Mach reflection calculations, while we virtually only began to resolve the double Mach reflection regime with our finest grid. For example, for double Mach reflection we should expect to perform two additional consistent refinements of our current fine meshing scheme to better examine the empirical order of convergence of the calculations, as well as to attempt an error extrapolation analysis. While such large calculations were beyond our scope for this study, they are possible in future work. At any rate, the absence of satisfactory grid convergence introduces additional uncertainty in our calculated results.

We believe that our current work is successful enough to serve as a starting point for both Arbitrary Lagrange Eulerian and Adaptive Mesh Refinement (AMR) Eulerian calculations of some or all of the same shock reflection experiments. This may be the subject of future work on this problem using ALEGRA.

Our present work does not appear to call into question the accuracy of the ideal gas model in simulating these shock reflection experiments. Nonetheless, performing assessments where non-ideal gases are important is an important step in the direction of the kind of plasma physics that must be modeled for Z-pinch applications. There is a body of experimental work that illustrates the influence of non-ideal gas phenomena in shock reflections (Ben-Dor and Glass, 1979). The associated data are sensitive, in particular, to molecular dissociation, and include quantitative isopycnic interferogram contours. These data are of interest for future ALEGRA validation assessments, especially for AMR calculations. Such experiments need to be modeled using a closer approximation to the actual experimental conditions than the simpler scaling approach used in this report, which mimicked the approach taken by Sandoval (1984). This is because any exploration of non-ideal gas effects will be sensitive to the real temperatures in the experiments, and so simulations will need to more closely match the believed experimental thermal conditions.

References

1. F. L. Addessio, et al. (1986), "CAVEAT: A Computer Code for Fluid Dynamics Problems with Large Distortion and Internal Slip," Los Alamos National Laboratory, LA-10613-MS.

2. G. Ben-Dor and I. I. Glass (1979), "Domains and Boundaries of non-stationary Shock-wave Reflexions. 1. Diatomic Gas," J. Fluid Mechanics, Vol. 92, part 3, 459-496.

3. G. Ben-Dor (1992), Shock Wave Reflection Phenomena, Springer-Verlag, New York.

4. D. J. Benson (1992), "Computational Methods in Lagrangian and Eulerian Hydrocodes," Comp. Methods Appl. Mech. Engng., Vol. 99, No. 2-3, 235-294.

5. Computational Engineering International (2001), Ensight User Manual for Version 7.3, Apex, North Carolina.

6. R. Courant and K. O. Friedrichs (1948), Supersonic Flow and Shock Waves, Interscience-John Wiley, New York.

7. CUBIT Development Team (1994), "CUBIT Mesh Generation Environment Volume 1: Users Manual," Sandia National Laboratories, SAND94-1100.

8. R. G. Easterling (2001), "Measuring the Predictive Capability of Computational Models: Principles and Methods, Issues and Illustrations," Sandia National Laboratories, SAND2001-0243.

9. F. H. Harlow and A. A. Amsden (1970), "Fluid Dynamics: An Introductory Text," Los Alamos National Laboratory, LA-4100.

10. W. Heilig and H. Reichenbach (1984), "Model Test Investigation of Shock Wave Reflection With The Aid of High Speed Shadow-Schlieren Visualization and Pressure Gauges," SPIE Proceedings, Vol . 491, High Speed Photography, 583-591.

11. L. F. Henderson (1982), "Exact Expressions for Shock Reflection Transition Criteria in a Perfect Gas," Zeitschrift fur Angewandte Mathematik und Mechanik, Vol. 62, No. 6, pp. 258-261.

12. R. G. Hills and T. G. Trucano (2001), "Statistical Validation of Engineering and Scientific Models With Application to CTH," Sandia National Laboratories, SAND2001-0312.

13. T. J. R. Hughes (1987), The Finite Element Method, Prentice-Hall, Inc., Englewood Cliffs, NJ.

14. T. Mehlhorn, C. Garasi, and T. Trucano (2000), unpublished work.

15. J. S. Peery and D. E. Carroll (2000), "Multi-Material ALE Methods In Unstructured Grids," Comput. Methods Appl. Mech. Engrg., Vol. 187, 591-619.

16. M. Pilch, T. Trucano, J. L. Moya, G. Froehlich, A. Hodges, and D. Peercy (2000), "Guidelines for Sandia ASCI Verification and Validation Plans – Content and Format: Version 2.0," Sandia National Laboratories, SAND2000-3101.

17. Research Systems, Inc. (1998), Using IDL, Boulder Colorado.

18. R. D. Richtmyer and K. W. Morton (1967), Difference Methods for Initial-Value Problems, 2nd Edition, Interscience, New York.

19. P. J. Roache (1998), Verification and Validation in Computational Science and Engineering, Hermosa Publishers, Albuquerque, New Mexico.

20. C. J. Roy, M. A. McWherter-Payne, and W. L. Oberkampf (2000), "Verification and Validation for Laminar Hypersonic Flow Fields," Fluids 2000, 19-22 June 2000, Denver, Colorado, AIAA 2000-2550.

21. C. J. Roy (2001), "Grid Convergence Error Analysis for Mixed-Order Numerical Schemes," AIAA Paper 2001-2606.

22. D. L. Sandoval (1987), "CAVEAT Calculations of Shock Interactions," Los Alamos National Laboratory, LA-11001-MS.

23. R. M. Summers, *et al*. (1997), "Recent Progress in ALEGRA Development and Application to Ballistic Impacts," Int. J. Impact Engng., Vol. 20, 779-788.

24. E. F. Toro (1999), Riemann Solvers and Numerical Methods for Fluid Dynamics, 2nd Edition, Springer-Verlag, New York.

25. T. G. Trucano, M. Pilch, and W. Oberkampf (2001), "Principles for Experimental Validation of ASCI Code Applications," in progress.

Appendix A: Traceability Information

A.1 Mesh Generation

Sample CUBIT input deck

```
############## USER DEFINED VARIABLES ##########
### specify wedge angle
# { ang = 40 }   ## angle
### specify geometry size
# { w   = 1.5 }        # width of brick
# { d1  = 4.   }       # depth of bottom brick
# { d2  = 0.2 }        # depth of middle  brick
# { d3  = 1.   }       # depth of top brick
# { d4  = 2.   }       # depth of rotated brick
# { h   = 1.    }      # height of brick
### specify mesh resolution size
# { m1  = 300 }       # of elements along side of bottom brick
# { m2  = 264 }       # of elements along the width
# { m3  = 60   }      # of elements along middle brick
# { m4  = 400 }       # of elements along the wedge
### specify mesh bias size
# { bias1  = 1.0095 }       # for elements on bottom brick
# { bias2  = .9985   }      # for elements on top brick

################################################

journal off

brick width {w} depth {d1} height {h}
brick width {w} depth {d2} height {h}
body 2 move x 0 y 2.1 z 0
brick width {w} depth {d3} height {h}
body 3 move x 0 y 2.7 z 0
brick width {w} depth {d4} height {h}
body 4 move x 0 y 3.2 z 0
rotate body 4 angle {ang} vertex 28 vertex 31
intersect body 3 with body 4

imprint all
merge all

curve 4  2  14  interval {m1}
curve 1  3  interval {m2}
curve 13 15 interval {m3}
curve 59 57 interval {m4}
```

```
curve 1 scheme bias {bias1} start vertex 2
curve 3 scheme bias {bias1} start vertex 3
curve 59 scheme bias {bias2} start vertex 11
curve 57 scheme bias {bias2} start vertex 10

mesh surface 1 7 30
draw surface 1 7 30

###### SETUP THE GENESIS OUTPUT ##################
block 1 surface 1
block 1 Element Type quad
block 2 surface 7 30
block 2 Element Type quad
sideset 1 curve 4
nodeset 1 curve 4
sideset 2 curve 1 13 57
nodeset 2 curve 1 13 57
sideset 3 curve 53
nodeset 3 curve 53
sideset 4 curve 59
nodeset 4 curve 59
sideset 5 curve 15 3
nodeset 5 curve 15 3

export genesis "1.37_40.gen" dimension 2
exit
```

A.2 ALEGRA Input

Sample ALEGRA input deck

```
$----------------------------------BEGIN_QA-----------------------------------------
$ ID: 1.37_40
$ Title:     mach1.37 caveat problem with 40 degree wedge
$ Category:     Verification and Validation
$ Physics:      hydrodynamics
$ Dimension:    2D
$ Owner:        Mary I.  Chen
$
$ Description:a column of gas impacts ideal gas surounding a wedge.  A
$     shock then travels up the wedge.  For this problem, there is a
$     1.37 mach number and 40 degree wedge
$-----------------------------------END_QA-------------------------------------------

title 1.37_40

hydrodynamics

  time step scale 0.6
```

```
  maximum initial time step 1.e-5

  pronto artificial viscosity
   linear 0.1
   quadratic 2.0
  end

  block 1
    material 1
    eulerian mesh
  end

  block 2
    material 2
    eulerian mesh
  end

  no displacement: nodeset 2 x
  no displacement: nodeset 3 x
  no displacement: nodeset 3 y
  no displacement: nodeset 4 x
  no displacement: nodeset 4 y
  no displacement: nodeset 5 x

  initial block velocity, block = 1, y = .53
  initial block velocity, block = 2, y = 0.0

end

termination time 0.7
Emit output, time interval=0.01
Emit plot,   time interval=0.1

plot variable
 pressure: avg
 coordinates
 density: avg
 artificial viscosity
end

material 1       IDGAS
  model  = 1
  density 1.64  $g/cm3
  temperature 369.562 $kelvin
end

material 2       IDGAS
  model  = 1
  density 1.0  $g/cm3
  temperature 300.  $kelvin
end

model 1 ideal gas
  gamma   = 1.4
  cv      = 5.953E-3
```

```
  rho ref = 1.0
  tref    = 300.0
end

exit
```

A.3 Post-Processing Discussion

Sample IDL input deck for $deltap_r/deltap_{inc}$

This IDL script corresponds to Fig 3.2 (ALEGRA and experimental data for Mach 3.36 calculation) in the report. First, IDL reads in the EXODUS II file and extracts the variable of interest: pressure. Then IDL reads in x-y data files for the theoretical and experimental data. In the next section, IDL is extracting the data along the wedge. Then, within the data of this plot, the maximum pressure is extracted. Data points before or behind the maxiumum can be easily chosen. After the desired pressures are gathered, they are used in Eq 3.1 and plotted against their respective incident wedge angles. Then the experimental data with their respective error bars are plotted on top of the existing ALEGRA data.

```
path = '/pr/weekly/michen/cartesian_wedge/mach3.36/'
path1 = '/home/michen/tim/caveat/cartesian_wedge/dig_data/mach3.36'
path2 = '/home/michen/tim/caveat/cartesian_wedge/mach3.36/pro_high_res'

;startgif, file =  'test'

set_plot, 'x'
popt='y
if (popt eq 'y') then begin
set_plot,'ps'
xpage=17
ypage=15
device, xsize=xpage,ysize=ypage, $
    filename= path2 + '/delta_p_rigged.ps'
endif

s1=readexo(file=path+'/40_degrees/goodres/3.36_40.exo', block=[2], $
 var='PRESSURE', /alltime, /eul)
s2=readexo(file=path+'/45_degrees/goodres/3.36_45.exo', block=[2], $
 var='PRESSURE', /alltime, /eul)
s3=readexo(file=path+'/50_degrees/goodres/3.36_50.exo', block=[2], $
 var='PRESSURE', /alltime, /eul)
s4=readexo(file=path+'/55_degrees/goodres/3.36_55.exo', block=[2], $
 var='PRESSURE', /alltime, /eul)

readcol, path1+'/file1_theo1', theox1, theoy1
readcol, path1+'/file1_theo2', theox2, theoy2
```

```
readcol, path1+'/experimental', expx, expy

numelem = n_elements(expx)
lasttime=n_elements(s1.time)-1

rows1 = uniq(s1.coord_y(*,0), sort(s1.coord_y(*,0)))
n1=n_elements(rows1)
i=0
row1=dblarr(n1)
b1=dblarr(n1)
while (i lt n1) do begin
  row1= where( s1.coord_y(*,0) eq s1.coord_y(rows1(i),0) )
  p1=n_elements(row1)-1
  b1(i) = row1(p1)
  i = i + 1
endwhile
a1=where(b1 ne b1(0))
place1=b1(a1)

m1=where(s1.data(place1,lasttime) eq max(s1.data(place1,lasttime)))
ind1=m1-11
ind11=m1+13
max1=s1.data(place1(ind1),lasttime)
max11=s1.data(place1(ind11),lasttime)
pr1 = max1-0.714
pr11 = max11-0.714
pinc1 =  9.29-0.714
val1 = pr1/pinc1
val11 = pr11/pinc1
print, 'val1 = ', val1
print, 'val11 = ', val11

lasttime2=n_elements(s2.time)-1

rows2 = uniq(s2.coord_y(*,0), sort(s2.coord_y(*,0)))
n2=n_elements(rows2)
i=0
row2=dblarr(n2)
b2=dblarr(n2)
while (i lt n2) do begin
  row2= where( s2.coord_y(*,0) eq s2.coord_y(rows2(i),0) )
  p2=n_elements(row2)-1
  b2(i) = row2(p2)
  i = i + 1
endwhile
a2=where(b2 ne b2(0))
place2=b2(a2)

m2=where(s2.data(place2,lasttime2) eq max(s2.data(place2,lasttime2)))
ind2=m2-11
ind22=m2+13
max2=s2.data(place2(ind2),lasttime2)
max22=s2.data(place2(ind22),lasttime2)
pr2 = max2-0.714
pr22 = max22-0.714
```

```
pinc2 =  9.29-0.714
val2 = pr2/pinc2
val22 = pr22/pinc2
print, 'val2 = ', val2
print, 'val22 = ', val22

lasttime3=n_elements(s3.time)-1

rows3 = uniq(s3.coord_y(*,0), sort(s3.coord_y(*,0)))
n3=n_elements(rows3)
i=0
row3=dblarr(n3)
b3=dblarr(n3)
while (i lt n3) do begin
  row3= where( s3.coord_y(*,0) eq s3.coord_y(rows3(i),0) )
  p3=n_elements(row3)-1
  b3(i) = row3(p3)
  i = i + 1
endwhile
a3=where(b3 ne b3(0))
place3=b3(a3)

m3=where(s3.data(place3,lasttime3) eq max(s3.data(place3,lasttime3)))
ind3=m3
max3=s3.data(place3(ind3),lasttime3)
pr3 = max3-0.714
pinc3 =  9.29-0.714
val3 = pr3/pinc3
print, 'val3 = ', val3

lasttime4=n_elements(s4.time)-1

rows4 = uniq(s4.coord_y(*,0), sort(s4.coord_y(*,0)))
n4=n_elements(rows4)
i=0
row4=dblarr(n4)
b4=dblarr(n4)
while (i lt n4) do begin
  row4= where( s4.coord_y(*,0) eq s4.coord_y(rows4(i),0) )
  p4=n_elements(row4)-1
  b4(i) = row4(p4)
  i = i + 1
endwhile
a4=where(b4 ne b4(0))
place4=b4(a4)

m4=where(s4.data(place4,lasttime4) eq max(s4.data(place4,lasttime4)))
ind4=m4-4
max4=s4.data(place4(ind4),lasttime4)
pr4 = max4-0.714
pinc4 =  9.29-0.714
val4 = pr4/pinc4
print, 'val4 = ', val4

errorplus = [ .583, .603, .601, .668, .801, .653, .442, .399, .361, $
```

```
            .657, .592, .525, .492, .447, .502, .505, 0., .324]
errorminus = [.713, .792, .603, .582, .515, .521, .398, .421, .442, $
     .588, .657, .653, .503, .551, .350, .392, 0., .246]

errorplus = errorplus /  5.461
errorminus = errorminus /  5.461

j = 0
l = 0
m = 0
line = dblarr(numelem,2,2)
top = dblarr(numelem,2,2)
bottom = dblarr(numelem,2,2)
while (j lt numelem) do begin
 while (errorplus(j) gt 0) do begin
  while (l eq 0) do begin
   while (m eq 0) do begin
    line(j,l,m) =  expx(j)
    top(j,l,m) =  expx(j) - .15
    bottom(j,l,m) = expx(j) - .15
    m = m + 1
   endwhile
   while (m eq 1) do begin
    line(j,l,m) =  expx(j)
    top(j,l,m) =  expx(j) + .15
    bottom(j,l,m) = expx(j) + .15
    m = m - 1
   endwhile
   l = l + 1
  endwhile
  while (l eq 1) do begin
   while (m eq 0) do begin
    line(j,l,m) =  expy(j) + errorplus(j)
    top(j,l,m) =  expy(j) + errorplus(j)
    bottom(j,l,m) = expy(j) - errorminus(j)
    m = m + 1
   endwhile
   while (m eq 1) do begin
    line(j,l,m) =  expy(j) - errorminus(j)
    top(j,l,m) =  expy(j) + errorplus(j)
    bottom(j,l,m) = expy(j) - errorminus(j)
    m = m - 1
   endwhile
   l = l - 1
  endwhile
  errorplus(j)=0
 endwhile
 j = j + 1
endwhile

errorplus = [ .583, .603, .601, .668, .801, .653, .442, .399, .361, $
            .657, .592, .525, .492, .447, .502, .505, 0., .324]
errorplus = errorplus / 12.879

; real x=[40, 45, 50, 55]
```

```
x=[50, 45, 50, 45, 40, 35]
y=[val1, val2, val11, val22, val3, val4]

plot, x, y, psym = 4, $
xtitle = 'incident angle', $
ytitle = 'delta p_r / delta p_inc', $
xrange = [30, 55], /xst, $
yrange = [1,6], /yst
oplot, theox1, theoy1, linestyle = 0
oplot, theox2, theoy2, linestyle = 0
oplot, expx, expy, psym = 6, symsize = .4
oplot, line(1,0,*), line(1,1,*), linestyle = 0

i = 0
while (i lt numelem) do begin
  oplot, line(i,0,*), line(i,1,*), linestyle = 0
  oplot, top(i,0,*), top(i,1,*), linestyle = 0
  oplot, bottom(i,0,*), bottom(i,1,*), linestyle = 0
  i = i + 1
endwhile

linestyle=[0]
psym=[4,6]
position =[.62, .87]
legtet=['ALEGRA', 'Experimental', 'Analytic']
legend, legtet, psym=[psym,0], line=[-1,-1,linestyle], pos=position, /normal

;spng
;endgif
end
```

Distribution

EXTERNAL DISTRIBUTION

Charles E. Anderson
Southwest Research Institute
P. O. Drawer 28510
San Antonio, TX 78284-0510

Mary E. Chen (10)
1601 Holleman
Apt. C4
College Station, Texas 77840

Richard Hills (2)
College of Engineering, MSC 3449
New Mexico State University
P. O. Box 30001
Las Cruces, NM 88003

Hans Mair
Institute for Defense Analysis
Operational Evaluation Division
4850 Mark Center Drive
Alexandria VA 22311-1882

Dale Pace
Applied Physics Laboratory
Johns Hopkins University
111000 Johns Hopkins Road
Laurel, MD 20723-6099

D. E. Stevenson (2)
Computer Science Department
Clemson University
442 Edwards Hall, Box 341906
Clemson, SC 29631-1906

SANDIA INTERNAL

1	MS 1186	1674	T. A. Mehlhorn
1	MS 1186	1674	T. A. Brunner
1	MS 1186	1674	R. B. Campbell
1	MS 1186	1674	K. R. Cochrane
1	MS 1186	1674	M. P. Desjarlais
1	MS 1186	1674	T. A. Haill
1	MS 1186	1674	R. J. Lawrence
1	MS 1186	1674	R. W. Lempke
1	MS 1186	1674	B. V. Oliver
1	MS 1186	1674	S. A. Slutz
1	MS 1186	1674	R. A. Vesey
1	MS 0482	2131	R. S. Baty
1	MS 9217	8950	M. L. Martinez-Canales
1	MS 9217	8950	P. D. Hough
1	MS 0847	9124	S. F. Wojtkiewicz
1	MS 0824	9130	J. L. Moya
1	MS 0828	9133	M. Pilch
1	MS 0828	9133	K. J. Dowding
1	MS 0828	9133	W. L. Oberkampf
1	MS 0557	9133	T. L. Paez
1	MS 0828	9133	V. J. Romero
1	MS 0557	9133	A. Urbina
1	MS 0835	9140	J. M. McGlaun
1	MS 0835	9142	J. S. Peery
1	MS 0321	9200	W. J. Camp
1	MS 0847	9211	S. A. Mitchell
1	MS 0847	9211	M. S. Eldred
1	MS 0847	9211	A. A. Giunta
20	MS 0819	9211	T. G. Trucano
1	MS 0847	9211	B. G. vanBloemen Waanders
1	MS 1110	9214	D. E. Womble
1	MS 0310	9220	R. W. Leland
1	MS 0318	9230	P. Yarrington
1	MS 0819	9231	E. A. Boucheron
1	MS 0819	9231	K H. Brown
1	MS 0819	9231	K. G. Budge
1	MS 0819	9231	S. P. Burns
1	MS 0819	9231	D. E. Carroll
1	MS 0819	9231	M. A. Christon
1	MS 0819	9231	R. R. Drake
1	MS 0819	9231	A. C. Robinson
1	MS 0819	9231	M. K. Wong
1	MS 0820	9232	P. F. Chavez
1	MS 0820	9232	M. E. Kipp
1	MS 0820	9232	S. A. Silling
1	MS 0819	9232	R. M. Summers
1	MS 0820	9232	P. A. Taylor
1	MS 0820	9232	J. R. Weatherby
1	MS 0316	9233	S. S. Dosanjh
1	MS 1111	9233	J. N. Shadid
1	MS 0316	9235	J. B. Aidun
1	MS 0316	9235	H. P. Hjalmarson
1	MS 0139	9905	S. E. Lott
1	MS 0829	12323	B. M. Rutherford
1	MS 0638	12326	D. E. Peercy
1	MS 9018	8945-1	Central Technical Files
2	MS 0899	9616	Technical Library
1	MS 0612	9612	Review & Approval Desk For DOE/OSTI